

M.J. Leyland, M.N.A. Beurskens, L. Frassinetti, T. Osborne, P.B. Snyder,
C. Giroud, S. Jachmich, G. Maddison, P. Lomas, C. Perez von Thun,
S. Saarelma, G. Saibene, K.J. Gibson and JET EFDA contributors

Pedestal Study in Dense High δ ELMy H-mode Plasmas on JET with the Carbon Wall

“This document is intended for publication in the open literature. It is made available on the understanding that it may not be further circulated and extracts or references may not be published prior to publication of the original when applicable, or without the consent of the Publications Officer, EFDA, Culham Science Centre, Abingdon, Oxon, OX14 3DB, UK.”

“Enquiries about Copyright and reproduction should be addressed to the Publications Officer, EFDA, Culham Science Centre, Abingdon, Oxon, OX14 3DB, UK.”

The contents of this preprint and all other JET EFDA Preprints and Conference Papers are available to view online free at www.iop.org/Jet. This site has full search facilities and e-mail alert options. The diagrams contained within the PDFs on this site are hyperlinked from the year 1996 onwards.

Pedestal Study in Dense High δ ELMy H-mode Plasmas on JET with the Carbon Wall

M.J. Leyland¹, M.N.A. Beurskens², L. Frassinetti³, T. Osborne⁴, P.B. Snyder⁴,
C. Giroud², S. Jachmich⁵, G. Maddison², P. Lomas², C. Perez von Thun⁶, S. Saarelma²,
G. Saibene⁷, K.J. Gibson¹ and JET EFDA contributors*

JET-EFDA, Culham Science Centre, OX14 3DB, Abingdon, UK

¹*York Plasma Institute, Department of Physics, University of York, Heslington, York, YO10 5DD, UK*

²*EURATOM-CCFE Fusion Association, Culham Science Centre, OX14 3DB, Abingdon, OXON, UK*

³*Division of Fusion Plasma Physics, Association EURATOM-VR, KTH, SE-10044 Stockholm, Sweden*

⁴*General Atomics, PO Box 85608, San Diego, California 92186-5608, USA*

⁵*Laboratory for Plasma Physics, ERM/KMS, EURATOM-Association "Belgian State", Belgium*

⁶*Max-Planck-Institut für Plasmaphysik, EURATOM-Association IPP, Garching, Germany*

⁷*FUSION FOR ENERGY Joint Undertaking, 08019 Barcelona, Spain*

** See annex of F. Romanelli et al, "Overview of JET Results",
(24th IAEA Fusion Energy Conference, San Diego, USA (2012)).*

ABSTRACT

We present the results from a new fuelling scan database consisting of 15 high triangularity ($\delta \sim 0.41$), Type I ELMy H-mode JET plasmas. As the fuelling level is increased from low, ($\Gamma_D \sim 0.2 \times 10^{22} \text{ e/s}$, $n_{e,\text{ped}}/n_{\text{gw}}=0.7$), to high dosing ($\Gamma_D \sim 2.6 \times 10^{22} \text{ e/s}$, $n_{e,\text{ped}}/n_{\text{gw}}=1.0$) the stored thermal energy shows no degradation. The ELM frequency decreases as density increases due to increased inter-ELM losses as shown by a slower build-up of stored energy for a high fuelling pulse in comparison to a low fuelling pulse. Consequently the ELMs at higher fuelling are referred to as ‘mixed Type I/II’ as opposed to ‘pure Type I’. These findings are consistent with previous studies [30], however the pulses in the new database are better diagnosed and most notable have pedestal measurements provided by the JET High Resolution Thomson Scattering (HRTS) system. We continue by presenting, for the first time, the role of pedestal structure, as quantified by a least squares $m \tanh$ fit to the HRTS profiles, on the performance across the fuelling scan. The pedestal pressure increases throughout the ELM cycle for low and high fuelling pulses. The pedestal width narrows and peak pressure gradient increases during the ELM cycle for a low fuelling pulse, whereas at high fuelling the pedestal width and peak pressure gradient saturates towards the latter half of the ELM cycle. An ideal MHD stability analysis shows that both low and high fuelling plasmas move from stable to unstable approaching the ideal ballooning limit of the finite peeling ballooning stability boundary. On DIII-D and MAST the pedestal width increases whilst the peak pressure gradient remains constant during an ELM cycle, as expected from the leading pedestal model, EPED. Therefore the new JET fuelling scan database is used for a comparison with EPED predictions. EPED self-consistently predicts the pre-ELM width and height with an accuracy of 20%. On average EPED agrees well with experimental measurements however when presented as a function of pedestal density experiment and model show opposing trends. The experimental pre-ELM pressure pedestal height increases by $\sim 20\%$ and the width widens by $\sim 55\%$, in poloidal flux space, for a high fuelling pulse in comparison to low fuelling pulse. The increase in pedestal pressure at high fuelling is attributed to the wider pedestal as the steep pressure gradient can be sustained over a large region at the plasma edge. In contrast EPED predicts a decrease of 25% in pedestal pressure and a decrease in pedestal width of 20% in flux space. We give two possible explanations for the disagreement. First, EPED under predicts the critical density, which marks the transition from kink-peeling to ballooning limited plasmas. Second, the stronger broadening of the experimental pedestal width than predicted by EPED is an indication that other transport related processes contribute to defining the pedestal width such as enhanced inter-ELM transport as observed at high fuelling, for mixed Type I/II ELMy pulses.

1. INTRODUCTION

The ITER baseline scenario is a Type I ELMy H-mode [15]. An H-mode is a high confinement mode of operation that is believed to arise due to the suppression of edge turbulence, resulting in an Edge Transport Barrier (ETB). A consequence of the ETB is the formation of a steep pressure

gradient at the plasma edge called the pedestal. The pressure pedestal height is limited by Edge Localised Modes (ELMs). ELMs are a periodic relaxation of the pedestal due to reaching a critical pedestal width and height, thought to be associated with crossing the Peeling Ballooning (PB) stability boundary [4]. The plasma core performance is strongly linked to the pressure pedestal height [15].

ITER will be considerably larger than current machines, operating at higher temperature and density. ITER will also be the first machine to have a significant fusion alpha particle fraction, contributing towards plasma heating. To improve the understanding of the ITER baseline scenario, research on current machines is focused on characterising regimes approaching the operational parameters of ITER. On JET, a discharge cannot simultaneously achieve ITER-like temperature and density. Instead separate studies investigate each operational parameter. For example, high temperature, low collisionality JET plasmas have been addressed [21]. Also of interest are dense plasmas, comparable to the Greenwald density.

Reference [14] states that at high density, with gas puff fuelling, it is difficult to maintain confinement in the Type I ELMy H-mode. A possible solution is to increase the degree of plasma shaping; more specifically the triangularity [16]. Dense, high triangularity ITER-like plasmas have been investigated by [30] on JET and are the focus of this paper. The key findings in [30] are, first, there was little degradation of stored energy when fuelled up to a pedestal density normalised to the Greenwald density ($n_{e,ped}/n_{GW} \sim 1$). Second, the Type I ELM frequency decreased with increasing pedestal density. And finally, the inter-ELM heat losses increased at high pedestal density, $n_{ped}/n_{GW} > 0.7$, thought to be due to a transition from a pure Type I to a mixed Type I/II ELMy regime.

The 2002 study was limited by diagnostic capabilities and consequently there remained some unanswered questions with respect to the role of pedestal structure to the change in performance. This can now be addressed using the JET High Resolution Thomson Scattering (HRTS) system [24], installed in 2005. In this paper, a new database is presented consisting of 15 dense high triangularity ELMy H-mode JET plasmas, comparable to [30], with good diagnostic coverage. The aim of this study is to utilise the HRTS electron temperature and density profiles to quantify the pre-ELM pedestal structure and the pedestal evolution during the ELM cycle. These measurements facilitate a PB stability analysis and a comparison to a predictive ITER relevant pedestal pressure model.

The focus of Section 2 and Section 3 is to show that the 2002 and new databases are comparable before going on, to present the new pedestal measurements. In Section 2, there is a detailed description and comparison of the two databases. Then the plasma performance of the new database is presented. Section 3 focuses on the transition from a pure Type I to a mixed Type I/II ELMy regime at high fuelling, as originally observed in the 2002 study [30].

Section 4 studies the electron temperature and density pedestal width and height determined by fitting a modified hyperbolic tangent (mtanh) function to HRTS profiles. Furthermore the inter-ELM evolution of the pedestal structure is studied by fitting to profiles selected from a temporal window in various phases of the ELM cycle.

Section 5 presents the result of a pedestal stability code, MISHKA-1 [19]. MISHKA-1 calculates the position of the PB stability boundary and the proximity of the plasma edge to this boundary, using the experimental profiles. A sensitivity analysis to quantify the uncertainties associated with the operational points relative to the stability boundary is also presented. Then section 5 goes on to present a comparison of the pedestal measurements to the results from the EPED1 model [38,40]. EPED1 is designed to predict the pressure pedestal width and height for present and future devices. This comparison helps further test that model and interpret the observations. Section 6 discusses the conclusions.

2. DESCRIPTION OF DATABASE

2.1. PLASMA SCENARIOS

The JET pulses within the new database were obtained during experiments with a carbon fibre composite (CFC) wall before the installation of the current Be/W ITER-Like-Wall (ILW) [27]. A D₂ fuelling scan from $\Gamma_D \sim 0.2$ to 6.1×10^{22} el/s was performed over 15 single null, Type I ELMy H-mode plasmas as described in [9, 17]. The high triangularity plasma scenarios for the 2002 and present study are compared in Table 1.

The two scenarios have similar plasma current, toroidal magnetic field strength, Neutral Beam Injection (NBI) heating power and gas fuelling capabilities. There is a small variation in triangularity due to the most notable difference between the two scenarios, the divertor configuration.

Figure 1 shows the EFIT equilibrium reconstruction for JET Pulse Number (JPN): 52014, from the 2002 study; and 79503, from the current study. The divertor geometry shown by Figure 1b is the Septum Divertor (SD) configuration, used in the 2002 study. The divertor geometry shown by Figure 1a and c is the Load Bearing Septum Replacement Plate (LBSRP) divertor configuration, as used in the current study. When operating with the LBSRP divertor an optimisation of plasma volume was possible due to achieving magnetic configurations with a lowered X-point position. The configuration chosen for this study is optimised for both volume and a choice of triangularity (~ 0.41) at which good confinement at high density was found.

2.2. DIAGNOSTIC SETUP

As previously mentioned, the 2002 study [30] was limited by diagnostic capabilities. The maximum electron density of the plasmas in [30] was $\sim 10^{20} \text{ m}^{-3}$, which is greater than the density cut-off for ECE emission, $\sim 8.5 \times 10^{19} \text{ m}^{-3}$. As a result the ECE heterodyne radiometer could not provide pre-ELM temperature profiles. However, currently the JET HRTS system can measure temperature and density profiles throughout the ELM cycle. The system utilises a 5J Q-switched Nd:YAG laser ($\lambda = 1064 \text{ nm}$) with a 20ns pulse duration and a 20Hz repetition rate across the entire JET pulse (~ 800 profiles) [24, 8]. The HRTS line-of-sight in the outer midplane is indicated by the green line in Figure 1a.

During the campaign the spatial resolution of the HRTS system was improved from a Full

Width Half Maximum (FWHM) instrument function of $\sim 22\text{mm}$ to $\sim 1\text{mm}$ [8]. Four out of the 15 plasmas have higher spatial resolution and are indicated by differently coloured symbols in the rest of the paper.

2.3. PLASMA CONFINEMENT

Figure 2 shows the evolution of key plasma parameters for a low fuelling ($0.2 \times 10^{22}\text{el/s}$, in blue) and a high fuelling pulse ($2.6 \times 10^{22}\text{el/s}$, in red) where both have high resolution HRTS coverage. And therefore these same two pulses will later be used for detailed profile analysis (Section 4).

The selected stationary region of a pulse is indicated by the coloured region of each trace in Figure 2. Plasma parameters are averaged over this region and as discussed later, HRTS profiles are selected for further analysis within this region.

Figure 2 shows for a similar input power ($P_{\text{NBI}} \sim 15\text{MW}$) both pulses have a comparable normalised beta ($\beta_{\text{N}} \sim 1.9$) and stored energy ($W_{\text{DIA}} \sim 6\text{MW}$). The two pulses have line averaged densities of 8.0 and $9.5 \times 10^{20}\text{m}^{-3}$ which is respectively 75% and 100% of the Greenwald density limit. As a consequence the confinement enhancement factor for these two pulses differ slightly ($H_{98} = 1.0$ and $H_{98} = 0.95$) due to the density dependence in the confinement scaling law (Figure 3). Figure 2h and 2i show that the ELM frequency reduces when the fuelling level is increased, as is typical for dense high triangularity plasmas in JET [30].

The 2002 and current optimised high δ Type I ELMy H-mode plasma scenarios, although different, both exhibit similar ELM behaviour and comparable confinement. The confinement enhancement factor (H_{98}) as defined [14] is used as a measure of the confinement performance. Figure 3a and 3b show H_{98} as a function of fuelling rate and the pedestal density normalised to the Greenwald density respectively.

Figure 3a shows H_{98} decreases by less than 10% up to a fuelling rate of $\Gamma_{\text{e}} \sim 4.8 \times 10^{22}\text{el/s}$. Above this fuelling rate there is a transition to a lower confinement state, so called compound ELMs [32], as indicated by a further reduction of H_{98} ($\sim 20\%$). The ELM frequency of the compound ELMy pulse is $\sim 100\text{Hz}$, whereas all the other pulses within the fuelling scan are between 5–25Hz. The ELM frequency is discussed further in section 3.

The variation of H_{98} for a given level of fuelling, see Figure 3a, implies the fuelling level does not sort the performance for these plasmas well. To achieve similar plasma parameters on different operational days the fuelling level has to be fine-tuned. This is to account for variations in wall conditioning and fuelling port location. A better sorting of the data is found with the pedestal density normalised to the Greenwald density ($n_{\text{e,ped}}/n_{\text{GW}}$), a plasma parameter, rather than the fuelling level (Γ_{D}), a machine parameter, as shown by Figure 3b. As pedestal density increases, H_{98} decreases between $n_{\text{e,ped}}/n_{\text{GW}} \sim 0.65 - 0.75$. This could be due to the scaling of H_{98} with density ($H_{98} \propto n_{\text{la}}^{-0.41}$ where n_{la} is the line average density) [14]. Above $n_{\text{e,ped}}/n_{\text{GW}} \sim 0.8$, H_{98} increases again, due to an apparent confinement improvement, up to a pedestal density of $n_{\text{e,ped}}/n_{\text{GW}} \sim 1.0$. The degraded performance of the compound ELMy pulse results in an intermediate pedestal

density ($n_{e,ped}/n_{GW} \sim 0.82$). Comparison of Figure 3a and 3b, indicate as the fuelling is increased the pedestal density initially increases, peaking at $n_{e,ped}/n_{GW} \sim 1.0$, corresponding to a fuelling rate of 2.6×10^{22} el/s. As the fuelling is further increased up to $\Gamma_D \sim 6.1 \times 10^{22}$ el/s, the pedestal density decreases due to the compound ELM transition.

Figure 3c and 3d show the total stored thermal energy (W_{th}) as a function of fuelling rate and pedestal density respectively. The stored thermal energy is calculated by correcting the measured diamagnetic energy (W_{DIA}) with the energy of the fast ions (W_{PET}) given by [13],

$$W_{th} = W_{DIA} - \frac{3}{2} W_{PET} \quad . \quad (1)$$

Similar to Figure 3a, Figure 3c shows a minimal degradation of stored thermal energy as fuelling increases until the compound ELM transition. In contrast to Figure 3b, Figure 3d does not show the initial decrease in W_{th} between $n_{e,ped}/n_{GW} \sim 0.65 - 0.75$, but similarly to H₉₈, W_{th} does increase at higher fuelling and then degrades for the compound ELM transition.

The pedestal stored energy, W_{ped} , is calculated by evaluating the volume integral of the pressure profile capped at the pressure pedestal height. The integral is given by:

$$W_{ped}(J) = \frac{3}{2} \int (p_i + p_e) dV \approx \frac{3}{2} \int e(n_i T_i + n_e T_e) dV \approx \frac{1}{4} \int e(13 - Z_{eff}) n_e T_e dV \quad (2)$$

where p_i and p_e are the ion and electron pressure profiles respectively in Pa; V is the plasma volume in m^3 ; e is a constant required for the conversion from eV to J and is equal to the elementary charge ($\sim 1.602 \times 10^{-19}$); n_i and n_e are the ion and electron density profiles respectively in m^{-3} ; T_i and T_e are the ion and electron temperature profiles respectively in eV; and Z_{eff} is the average effective atomic charge. The pressure profile is calculated from the product of an mtanh fit [2] to the density and temperature HRTS data. The HRTS data selected for the fits in Figure 3e and 3f are ELM averaged over the stationary phase of a pulse. Equation 2 assumes $T_i \sim T_e$, justified for all pulses discussed here due to their high density and therefore strong ion–electron heat exchange coupling. Z_{eff} is averaged over the stationary phase of each pulse within the fuelling database and is assumed constant in radius. Z_{eff} ranges from 1.5 to 2.1. The expression for W_{ped} utilises the following relationship between n_i and n_e assuming Carbon is the sole impurity,

$$n_i = \left(\frac{7 - Z_{eff}}{6} \right) n_e \quad (3)$$

The pedestal stored energy as calculated by equation (2) is shown in Figures 3e and 3f. In contrast to Figure 3a, Figure 3e shows as the fuelling is increased, the pedestal stored energy also increases and peaks at a fuelling rate of $\Gamma_D \sim 2.6 \times 10^{22}$ el/s. At higher fuelling the pedestal stored energy then decreases. Figure 3f shows the low fuelling pulses have low pedestal density and pedestal stored energy. The pedestal density and pedestal stored energy both peak at a fuelling of $\Gamma_D \sim 2.6 \times 10^{22}$ el/s. As the fuelling is further increased, towards the compound ELM transition, the pedestal

density and pedestal stored energy both degrade.

Figure 3g and 3h show the ratio of the pedestal stored energy to the total thermal stored energy ($W_{\text{ped}}/W_{\text{th}}$) as a function of fuelling rate and the pedestal density respectively. This ratio gives an indication of the profile peaking, which is the relative edge and core performance. The greater the core performance relative to the edge, the more peaked the profile. The profile peaking is not constant across the fuelling scan as $W_{\text{ped}}/W_{\text{th}}$ ranges from 0.27 at low pedestal density ($n_{\text{e,ped}}/n_{\text{GW}} \sim 0.65$) to 0.35 at high pedestal density ($n_{\text{e,ped}}/n_{\text{GW}} \sim 1.0$). To summarise, Figure 3b and 3d show for Type I ELMy pulses there is minimal degradation in overall performance (H_{08} and W_{th}) up to $n_{\text{e,ped}}/n_{\text{GW}} \sim 1$, in agreement with [30].

3. ELM CHARACTERISATION

The ELM type for the 2002 study was characterised as Type I ELMs at low fuelling and as mixed Type I/II ELMs at high fuelling levels [30].

A pure Type II ELMy regime is classified by the absence of large transient heat loads (Type I ELMs) and a minimal decrease in confinement (H_{08}) when compared to a Type I ELMy regime [26]. Type II ELMs produce a continuous power load on plasma facing components, similar to that of Type III ELMs. The degradation in confinement due to Type II ELMs is typically less than 10%, distinguishing them from a larger reduction in confinement of $\sim 20\text{--}30\%$ found in Type III ELMy regimes [32].

A transition from a Type I to a pure Type II ELMy regime is observed on AUG in single null configurations [44]. This transition is achieved by applying strong fuelling to exceed a collisionality threshold. Gas fuelling and plasma shaping, more specifically the proximity to Double Null (DN), are the two main methods of controlling the Type I to Type II transition [26].

JET results do thus far not show a pure Type II ELM regime in a single null configuration [28], but instead there is evidence for a mixed Type I/II ELMy regime for pulses with a high pedestal density where $n_{\text{e}} \geq 0.7n_{\text{GW}}$, as seen by [30]. A mixed Type I/II ELMy regime exhibits increased inter-ELM losses (Type II) between Type I ELMs. The key findings from the new fuelling scan database, which exhibits the same mixed Type I/II behaviour, are presented below focusing on the ELM frequency dependence, inter-ELM build up of stored energy and proximity to the LH threshold.

Figure 2h and 2i show the D_{α} emission for the low and high fuelling case respectively. The ELM frequency for a low and high fuelling pulse is 17.5Hz and 7.8Hz respectively. Figure 4 shows the ELM frequency for the entire database as a function of pedestal density. As observed by [30], the ELM frequency for the new database of high triangularity pulses decreases with increasing pedestal density.

The explanation given by [30] for the decrease in ELM frequency is that increased inter-ELM losses (Type II activity) at higher pedestal density, increases the time taken to reach the critical pressure and therefore reduces the Type I ELM frequency.

For the mixed Type I/II ELMy regime to account for the ELM frequency variation, it would be expected that the energy build-up for a pulse exhibiting Type II inter-ELM activity, a high fuelling pulse, would be slower in comparison to a low fuelling pulse.

Figure 5 compares the inter-ELM stored energy build-up of a high and low fuelling pulse as calculated from magnetic diagnostics. The build up after multiple ELM collapses are overlaid to improve temporal resolution, see Figure 5a. Figure 5b shows the result of normalising the ELM synchronised data to a 5–10ms post-ELM window and then applying a moving average. Figure 5a and b both show there is a difference in the build up between the two pulses and also that the build up of stored energy does not saturate.

The existence of mixed Type I/II ELMs is consistent with the decrease in ELM frequency across the fuelling scan although another factor which could influence the ELM frequency is the proximity to the L–H power threshold, above which a transition from L to H–mode occurs. In, for example, [31] the ELM frequency is shown to reduce when the input power approaches the L–H power threshold for a JET ELMy H–mode fuelling database.

The LH power threshold has been determined using the scaling derived from a multi machine database for P_{LH-08} , [18]. The total loss power is defined [18],

$$P_{loss} = P_{NET} - \frac{dW}{dt} \quad (4)$$

where P_{NET} is the total net input power and dW/dt is the rate of change in plasma stored energy. P_{NET} in MW is given by [13],

$$P_{NET} = P_{CX} + P_{ICRH} + P_{OHM} - P_{SHI} \quad (5a)$$

$$P_{CX} = P_{NBI} \left(1 - \frac{1}{100} \exp(3.35 - 0.667 \cdot \text{abs}|I_p| - 0.2n_{e,la}) \right) \quad (5b)$$

where P_{CX} in MW is the power deposited in the plasma due to NBI heating taking into account all losses, P_{ICRH} in MW is the input power due to Ion Cyclotron Resonant Heating (ICRH), P_{OHM} in MW is the input power due to ohmic heating, P_{SHI} in MW is the power lost due to NBI shine-through, P_{NBI} in MW is the input NBI power not taking into account losses, I_p in MA is the plasma current and $n_{e,la}$ in 10^{-19} m^{-3} is the line average electron density.

The LH threshold power described by [18] refers to the power required to access H–mode. In the calculation of P_{loss} in stationary H–modes, the term dW/dt varies strongly during the ELM cycle. For this reason dW/dt at the end of the ELM cycle (70–99%) has been used in the calculation as considered most relevant with respect to the ELM event.

Figure 6 shows the ratio of the total loss power (P_{loss}) to the LH threshold power (P_{LH-08}). Figure 6 shows that the ratio of P_{loss}/P_{LH-08} remains approximately constant, ~ 1.1 from low to high fuelling (comparing green datapoints) implying the ELM frequency is most likely independent of the proximity to the LH threshold.

In summary, the observations on the ELM regime in this paper are consistent with those in [30] and a transition from the pure Type I ELMs to a mixed Type I/II ELM regime is a most likely reason for the non-standard ELM behaviour. Following the convention as laid out in [30], the low and high fuelling example pulses referred to within this paper are termed as pure Type I and mixed Type I/II ELM H-modes.

4. PEDESTAL MEASUREMENTS

In section 2.2 we saw that the increase in stored thermal energy above $n_{e,ped}/n_{GW} = 0.8$ is largely due to an increase of the pedestal stored energy. To understand why the pedestal performance improves when the fuelling level is increased this section quantifies the behaviour of the H-mode pedestal within the new JET fuelling database, utilising electron temperature (T_e) and density (n_e) profiles produced by the JET HRTS system. The pedestal structure, i.e. the width and height, and pedestal dynamics are quantified by least squares mtanh fits to ELM synchronised HRTS profiles. These observations are used in Section 5 when evaluating the Peeling Ballooning stability and comparing experimental results to EPED1 predictions for the pedestal pressure.

4.1. PEDESTAL FITTING: MTANH AND LINEAR FORMS

For pulses within the new database, the Type I ELM period ranges from 25–150ms. The HRTS laser fires every 50ms therefore on average there are 1–2 profiles per ELM period. HRTS T_e and n_e profiles typically have 2–3 spatial points defining the pedestal region. To maximise the data selected for performing a fit, specifically the number of points defining the pedestal, profiles from the same phase of the ELM cycle are overlapped. Profiles within the last 70–99% of the ELM cycle, from a window spanning the stationary phase of a pulse (typically $\sim 2s$), are used to determine pre-ELM fits [2, 8]. The radial position of each profile is corrected according to the edge of the plasma to account for the dynamic variation of the plasma position during the pulse. The profiles are deconvolved using a numerically calculated instrument function taking into account the input setup of the polychromators [8]. The density and temperature profiles use a classic and weighted deconvolution technique respectively, [34]. Figure 7 shows the result of a least squares mtanh fit to determine the pedestal width and height. Figure 7a–d show the selected overlaid HRTS temperature and density profiles (open circles) and the corresponding mtanh fits (dashed lines) for the pure Type I pulse and mixed Type I/II pulse respectively as shown in Figure 2. Both the temperature and density pedestals are wider for the mixed Type I/II pulse in comparison to the pure Type I pulse. Further still, the pedestal temperature is smaller by $\sim 0.1keV$ (12%) whereas the pedestal density is significantly larger by $\sim 2.6 \times 10^{19} m^{-3}$ (37%), as a consequence the pedestal pressure increases by 20%

Beyond the extent of the foot of the mtanh fit function, see Figure 7, there is minimal data weakening the validity of the mtanh fit in this region. Least squares linear fits were performed on the same data selected for the mtanh fits to provide a comparison, see Figure 8 [35]. Figure 8a–d

show the linear fit to the selected overlaid HRTS temperature and density profiles for the pure Type I and mixed Type I/II pulse respectively. In agreement with the mtanh fit, the linear fits suggest the temperature and density pedestal is wider for the mixed Type I/II pulse in comparison to the pure Type I pulse. Further still, the pedestal temperature and pedestal density, determined from the linear fit, show a similar small decrease and significant increase respectively. In comparison to the mtanh fit the linear fit width is larger for both the temperature and density pedestal. The temperature pedestal height from the linear fit is marginally larger in comparison to the mtanh fit. Interestingly the density pedestal height is similar for the mtanh and linear fit due to the relatively flat core gradient accurately constraining the knee of the profile.

Figure 9 details a comparison of linear and mtanh fits for the temperature pedestal width, the density pedestal width, the temperature pedestal height and the density pedestal height. This comparison includes all pulses within the new JET fuelling database. As well as considering HRTS profiles from the last 70–99% of the ELM cycle, profiles within 0–10%, and 0–100% (i.e. all time windows) of the ELM cycle were also considered.

The linear density and temperature pedestal width is larger than the corresponding mtanh widths as shown by Figure 9a and b respectively, due to a difference in the definition of the pedestal widths for both fits. Similarly Figure 9c shows the linear temperature pedestal height is larger than the mtanh pedestal height. Figure 9d shows the density pedestal heights for the linear and mtanh fits are in good agreement. To summarise there are some deviations between pedestal widths and heights when comparing linear and mtanh fits, see Figure 9. These deviations are purely a consequence of the different fit functions. The data trends are still consistent.

Figure 9a and b show the post-ELM widths (orange data points) are larger than the pre-ELM widths (red data points) indicating both the density and temperature pedestal width narrows during the ELM cycles. The pedestal structure evolution is discussed in more detail in section 4.3.

4.2. PEDESTAL STRUCTURE

In this paper we refer to the pedestal structure as the width and height of the pedestal. The examples of mtanh and linear fits in the previous section, Figure 7 and 8 respectively, show for the mixed Type I/II pulse in comparison to the pure Type I pulse: the temperature and density pedestal widens; the pedestal temperature is lower and the pedestal density is higher. This section presents the measurements of the pre-ELM (70–99%) pedestal structure for all pulses within the new fuelling scan database.

Figure 10 shows the variation of pedestal width with respect to the pedestal density. The temperature and density widths for pulses with low (~22mm) resolution HRTS profiles, the orange points, are more scattered and have larger error bars in comparison to the pulses with high (~11 mm) resolution HRTS pulses, the green points. This is understandably so as the actual pedestal width, i.e. 1.5–2.0cm for the density and 2.0–3.0cm for the temperature pedestal, is of the same order as the width of the instrument function for the lower resolution cases [8]. The comparison

of relative scatter between low and high resolution HRTS pulses may be misleading due to there being more low resolution HRTS pulses. The high resolution data from Figure 10a and 10b shows evidence for the temperature and density pedestal widening as the pedestal density increases. The data set is limited due to no pulses with intermediate pedestal densities.

Figure 11 shows the pedestal temperature versus pedestal density for all pulses within the current fuelling database. The two main groups of pulses correspond to pure Type I (low fuelling) and mixed Type I/II (high fuelling) ELMy H-modes. The mixed Type I/II pulses have a lower pedestal temperature and higher pedestal density relative to the pure Type I pulses, see Figure 7. Further still, as indicated by the isobars, black dashed lines, the mixed Type I/II pulses have higher pedestal pressure. The pure Type I pulses are all between the lower (p_L) and central (p_C) isobars whereas the mixed Type I/II pulses are between the central (p_C) and upper (p_U) isobars. The degraded performance of the compound ELMy pulse is reflected in the lowest pressure pedestal due to a reduction in both T_e ($T_{ped} \sim 0.55\text{keV}$) and n_e ($n_e \sim 7.8 \times 10^{19} \text{m}^{-3}$).

4.3. PEDESTAL DYNAMICS

The HRTS profiles for two plasmas with high resolution data; a pure Type I and a mixed Type I/II pulse from the new JET fuelling database, have been windowed from 0–10%, 10–40%, 40–70% and 70–99% of the ELM cycle. The corresponding mtanh fits quantify the pedestal width and height for each region of the ELM cycle. The initial 0–10% of the ELM cycle can be considered as a transient recovery phase after the ELM crash. As a result the pedestal width and height from the fit corresponding to 0–10% of the ELM cycle may not follow a trend described by the rest of the data.

Figure 12a shows the evolution of the temperature and density pedestal width for a pure Type I and mixed Type I/II pulse. For both pulses the temperature and density pedestals jump from large post-ELM pedestal widths ($\Delta n_e \sim 5.0\text{--}5.7\text{cm}$, $\Delta T_e \sim 4.0\text{--}4.5\text{cm}$), corresponding to profiles from 0–10% of the ELM cycle, to smaller intermediate values ($\Delta n_e \sim 2.0\text{cm}$, $\Delta T_e \sim 3.0\text{cm}$). The pure Type I pulse then progressively narrows during the rest of the ELM cycle to pre-ELM widths of $\Delta n_e = 1.5\text{cm}$ and $\Delta T_e = 1.9\text{cm}$. In comparison, the pre-ELM widths for the mixed Type I/II pulse are $\Delta n_e = 2.1\text{cm}$ and $\Delta T_e = 2.9\text{cm}$ as the pedestal widths remain approximately constant for 10–40%, 40–70% and 70–99% of the ELM cycle. The inter-ELM evolution of the density pedestal width, as observed using HRTS, has been verified using Li-beam measurements at the plasma edge for a pure Type I ELMy pulse and mixed Type I/II ELMy pulse presented in this paper [7].

The evolution of the temperature and density pedestal height during the ELM cycle for a pure Type I and mixed Type I/II pulse is shown by Figure 12b. Initially the temperature pedestal height rapidly grows, slowing down towards the end of the ELM cycle and for the mixed Type I/II pulse the temperature pedestal height saturates. The density pedestal height, for both pulses, increases throughout the ELM cycle. Overall the pedestal pressure increases, for both pulses, during the ELM cycle. The pure Type I pulse is at relatively high temperature and low density in comparison to the mixed Type I/II pulse.

Figure 13a and b show the pressure profiles determined from the temperature and density mtanh fits corresponding to 0–10%, 10–40%, 40–70% and 70–99% of the ELM cycle. Figure 13c and d show the derivative of these pressure profiles with respect to the mid-plane radius. Figure 13 focuses on the two pulses considered throughout this paper. Figure 13a and c corresponds to the pure Type I pulse. Figure 13b and d corresponds to the mixed Type I/II pulse. The trends shown by Figure 12 can also be seen in Figure 13.

The pressure pedestal for the pure Type I pulse narrows during the ELM cycle, as clearly seen in Figure 13c. This is consistent with Figure 12a. The peak pressure gradient does not saturate during the ELM cycle. The position of the peak pressure gradient shifts radially outwards by $\sim 1.5\text{cm}$ during the ELM cycle suggesting the entire pedestal also moves radially outwards.

Disregarding the profile for the initial 0–10% of the ELM cycle, the pressure pedestal width is relatively constant for the mixed Type I/II pulse, see Figure 13d. Once again this is consistent with Figure 12a. The peak pressure gradient increases from 10–40% to 40–70% and then remains constant from 40–70% to 70–99%. The lack of variation in peak pressure gradient position suggests a minimal shift in pedestal position during the ELM cycle.

The evolution of the pedestal, as described above, can be compared to observations on other devices. At DIII–D a widening of the electron density, temperature and pressure pedestal during the ELM cycle was observed in plasmas with the so-called ITER baseline shape [11, 22]. This widening is consistent with a combined Kinetic Ballooning (KB) and PB model where the pedestal width increases during the ELM cycle following a KB gradient limit, until the ELM is triggered when the PB limit is reached [41]. Similar observations were found in MAST where there is also a widening of the pressure pedestal inbetween ELMs [5, 6]. The extent of the barrier is again found to be limited by KB modes and this was confirmed by local gyrokinetic analysis.

However, in the cases studied here, the inter-ELM evolution of the JET pedestal is different from that typically observed in other tokamaks such as DIII–D and MAST. In the analysis presented above the JET H-mode pedestal width narrows or saturates during the ELM cycle. Also in contrast to MAST initial gyro-kinetic analysis of JET Type I ELMy H-mode plasmas reveals that the inter-ELM pedestal evolution is typically in the 2nd stable regime for purely local KB modes [29].

5. COMPARISON WITH MODELS

5.1. PEDESTAL STABILITY ANALYSIS

Figure 14 shows the result of the PB stability analysis performed by MISHKA–1; an ideal MHD eigenvalue solver [19]. A detailed description of the analysis process is provided by [28]. To summarise, the input is a pressure profile calculated from the temperature and density mtanh fits, discussed in the previous section. The radial position of the profile is corrected such that the separatrix temperature is $\sim 100\text{eV}$, i.e. consistent with the two-point model for the power balance at the separatrix. The edge bootstrap current is calculated using the expression provided by [33] and the plasma equilibrium is self consistently calculated with the HELENA equilibrium solver [12].

The output, see Figure 14, is an operational point and a corresponding stability boundary in terms of the edge current (J_{sep}) and the dimensionless maximum pressure gradient (α_{max}) [20]. Both these parameters, if large, drive a plasma to be unstable with respect to ELMs. Figure 14a and 14b show operational points representing the state of a plasma during the ELM cycle for the pure Type I and mixed Type I/II pulses in Figure 7.

The blue region is stable, the red region is unstable and the black dashed line indicates the stability boundary ($\gamma = 0.03\omega_A$). The proximity of the point to the stability boundary indicates the stability of the plasma edge at the time corresponding to the input profile. The location of the stability boundary depends on the pedestal width therefore the stability boundary is re-calculated for each input profile.

Figure 14a and 14b show the stability boundary and operational point corresponding to the plasma state at the last 70–99% of the ELM cycle. The operational points for 0–10%, 10–40% and 40–70% have been also overlaid to give an indication of relative stability during the ELM cycle but the boundary strictly only applies to the 70–99% data point, the black star. The proximity of each operational point to its true boundary has been preserved by scaling the position of the operational point relative to the 70–99% boundary.

The pure Type I pulse becomes progressively more unstable during the ELM cycle, as expected from the pedestal evolution shown by Figure 12 and 13. The pre-ELM operational point for the pure Type I pulse is over the stability boundary, in the unstable region. The operational point for the mixed Type I/II pulse initially evolves towards the stability boundary until the last 40–70% and 70–99% of the ELM cycle. These two operational points are similar due to near identical input profiles provided to the code. The pure Type I and mixed Type I/II pulses are both most unstable to the $n = 15$ mode.

A sensitivity analysis has been performed to quantify the uncertainties. Variations in the input to MISHKA-1 have been implemented for the point corresponding to the last 70–99% of the pure Type I pulse, as shown by Figure 15.

The largest deviation from the 70–99% operational point for the pure Type I pulse, the black star shown by Figure 14a, is due to a 0.5% shift in normalised flux of the pressure profile. Figure 15a shows both the stability boundary and operational point have shifted closer together and therefore the plasma is not as deeply unstable. Also the operational point is on the ballooning boundary rather than the PB corner.

The total pressure profile, an input to MISHKA-1, is dependent on the effective atomic charge (Z_{eff}) through the ion density, see Equation (6).

$$p = n_e T_e \left(+ n_i n_e, Z_{\text{eff}} \right) T_i \quad (6)$$

Consequently any variation in Z_{eff} would influence the PB stability analysis. Experimentally in hydrogenic plasmas Z_{eff} is found to be ~ 2 due to impurities. Figure 15b shows there is a minimal

change in the position of the operational point when Z_{eff} is set to 1.

The results presented by Figure 14 all assume the ion temperature is equivalent to the electron temperature ($T_i = T_e$). This is not always the case, particularly in a low collisionality, highly NBI fuelled plasma. T_i can be constrained by matching the core and edge temperature gradient. The resulting flat ion temperature profile has a minimal effect on the stability analysis, see Figure 15c. The operational point moves marginally towards the ballooning region at low J_{sep} and high α .

To summarise, when quantifying the sensitivity of the PB stability analysis, a shift in normalised poloidal flux (0.5%) of the pressure profile resulted in the only significant deviation of the operational point. The operational point for the pure Type I pulse, for 70–99% of the ELM cycle, is still at critical stability. The physical interpretation of the stability analysis has not changed due to the sensitivity analysis. The variation in Z_{eff} and matching core and edge T_i gradient both result in minor deviations.

As shown by Figure 10 and 11, the mixed Type I/II pulse has a wider pedestal and is able to reach a higher pedestal pressure. In the context of PB theory there are two competing factors influencing the achievable pedestal pressure with respect to a variation in pedestal width. First, a wider pressure pedestal results in a lowering of the PB stability boundary due to PB modes becoming more unstable at lower pressure gradient. However, for a comparable pressure gradient, a wider pedestal can still result in an increased pedestal height. As the mixed I/II pulses from the new JET fuelling database reach a higher pressure when the pedestal widens this suggests the lowering of the stability limit is not the dominating factor.

5.2. EPED COMPARISON

The EPED model is designed to predict the pressure pedestal structure. The inputs to the model are eight scalar parameters, $B_t(\text{T})$ the toroidal magnetic field, $I_p(\text{MA})$ the plasma current, $R(\text{m})$ the major radius, $a(\text{m})$ the minor radius, δ the triangularity, κ the elongation, $n_{e,\text{ped}}(10^{19} \text{m}^{-3})$ the pedestal density and $\beta_{N,\text{global}}$ the global Troyon normalised β . EPED assumes the pedestal pressure will rise until constrained by the onset of two key instabilities, PB modes and KB modes. These instabilities provide two calculable constraints which when combined can be solved for the two unknowns, the pedestal height and width [38, 40, 42].

The PB stability boundary is evaluated by calculating the growth rate of intermediate toroidal mode numbers typically in the range of $n \sim 3\text{--}30$. This can be achieved using an ideal MHD code which in the context of EPED is generally ELITE [36, 43]. The PB stability boundary defines the maximum achievable pedestal height as a function of pedestal width which is assumed to be the same for both density and temperature. The PB calculation presented in the previous section relies on the experimental profiles to define the pedestal width, whereas for a predictive model a second condition is required, as provided by the onset of KB modes.

KB modes limit the pressure gradient within the edge barrier, in an approximately local sense. The pedestal can grow consistently with the KB modes until reaching the PB limit at which point

an ELM is triggered. The KB constraint is based upon the premise of strong KB mode turbulence, which when integrated across the entire edge barrier, results in a relationship between the pressure pedestal width in normalised poloidal flux (Δ) and the pedestal poloidal normalised pressure ($\beta_{pol,ped}$). In the full EPED1.62 model [40], this relationship is directly calculated for each case. In the simplified EPED1 model, this constraint takes the simple form,

$$\Delta \equiv \frac{1}{2} \left(\Delta_{n_e} + \Delta_{T_e} \right) = c_1 \cdot \sqrt{\beta_{pol,ped}} \quad (7)$$

where $\beta_{pol,ped}$ is calculated using the expression given by e.g [Beurskens 2011],

$$\beta_{pol,ped} = \frac{P_{ped}}{B_{pol}^2 / 2\mu_0} = \frac{P_{ped}}{(\mu_0 I_p / C)^2 / 2\mu_0} = \frac{2C^2 P_{ped}}{\mu_0 I_p^2} \quad (8)$$

Where p_{ped} is the plasma pressure in Pa, B is the magnetic field strength in T, I_p is the plasma current in A and C is the plasma circumference in m. In Equation (7) the average of the temperature and density pedestal width is used to define the total pedestal width. The value of c_1 can be calculated using the method described in [40], and generally is found to have a value in the range 0.06–0.09 for medium aspect ratio tokamaks.

The pedestal predictions from two versions of the EPED model, EPED1 and EPED1.62, are presented in this section. EPED1.62 has a more sophisticated implementation of the KB constraints as detailed in [40]. When considering the KB constraint, in the context of EPED1, c_1 in Equation (7) takes a constant value of 0.076. In EPED1.62 c_1 is calculated directly, and is a weakly varying function of parameters such as collisionality (ν^*) and aspect ratio (ϵ). A Ballooning Critical Pedestal (BCP) technique, see [44], is used to calculate c_1 . For the new fuelling database c_1 ranges between 0.072 and 0.078 with an average of 0.076. This is in good agreement with the value of c_1 used in EPED1.

Figure 16a shows a comparison between EPED1 (black dashed line) and EPED1.62 (blue shaded region) width predictions and the experimental width measurements as a function of predicted $\beta_{pol,ped}$. The ratio of predicted to observed pedestal width is 1.01 ± 0.23 for EPED1 and 1.00 ± 0.20 for EPED1.62. Therefore, on average there is a good agreement between the predicted and measured pedestal widths. However, the measured widths decrease with increasing predicted $\beta_{pol,ped}$, whereas EPED predicts an increase. In the experiments the plasmas with the wider pedestal reach an increased pedestal pressure and consequently a higher $\beta_{pol,ped}$. This is reflected in Figure 16b which shows the measured pedestal width increases with measured $\beta_{pol,ped}$ albeit with a stronger broadening than the $\sqrt{\beta_{pol,ped}}$ -prediction.

The EPED1 model has previously been compared to a large dataset of low and high triangularity baseline and hybrid discharges on JET [2, 3, 41]. These previous studies have found good statistical agreement with the model, with a ratio of predicted to observed pedestal pressure of 0.97 ± 0.21 . These previous comparisons are shown, along with a comparison to the new fuelling database

in Figure 17a. Figure 17b shows both the EPED1 (open red circles) and EPED1.62 (closed green diamonds) pedestal pressure predictions and the measured pedestal pressure (closed blue triangles) as a function of pedestal density for all Type I ELMy H-mode pulses within the new fuelling database. Again on average there is a good agreement between EPED predictions and the measurements as the ratio of predicted to observed pedestal pressure in the new fuelling database is 1.04 ± 0.22 for EPED1 and 1.04 ± 0.19 for EPED1.62. However, when presented as a function of pedestal density this highlights a systematic trend within the data. For this range of density, EPED1 and EPED1.62 both show a decrease in pedestal pressure as pedestal density increases whereas the experimental measurements show an increase.

More generally, for high triangularity discharges such as those in the new fuelling database, EPED predicts a pedestal pressure that first increases, and then decreases with density [37, 38]. We illustrate this by taking the EPED input parameters from discharge 79498, varying the pedestal density, and calculating the EPED predicted pedestal pressure as a function of density. As the pedestal density is increased, this results in an increasing collisionality at a given pressure. The resulting collisional suppression of the bootstrap current eventually leads to a transition from the kink/peeling limited regime (where EPED predicted pressure increases with density) to the primarily ballooning-limited regime (where EPED predicted pressure decreases weakly with density), as shown in Figure 18a. We can define a critical density at which this transition occurs, here $n_{e,\text{ped,crit}} \sim 6 \times 10^{19} \text{ m}^{-3}$. The corresponding EPED predicted pedestal pressure as a function of normalized density is shown in Figure 18b. The solid line shows the prediction for $Z_{\text{eff}} = 1.92$, the nominal value for 79498. Because the transition shown in Figure 18a is related to collision suppression of the bootstrap current, it correlates not just to density, but also to Z_{eff} . Reducing Z_{eff} from 1.92 to 1 (dashed line in Figure 18b) results in an increase of the critical density up to a Greenwald fraction near 1. It appears that, at higher pedestal density, EPED maybe under predicting the observed pedestal height due to under predicting the critical density at which the PB stability changes character from kink/peeling to PB limited. If the strong deuterium fuelling near the edge used to reach high density is reducing the value of Z_{eff} within the edge barrier, this could provide an explanation for the continued increase in pedestal pressure with density. Other possible explanations are under further investigation, including more accurate accounting of the impact of ion dilution and impurities on the bootstrap current. It is also important to note that strictly speaking the EPED model was designed for pure Type I ELMy H-mode plasmas. Consequently it may not be appropriate to perform an EPED comparison for all pulses within the new fuelling database. We note that if resistive effects or an effect associated with Type II ELMs were able to hold the pressure gradient slightly below the KB critical value, this would result in a prediction of a somewhat wider and higher pedestal [41], which would be qualitatively consistent with observations.

6. DISCUSSION AND CONCLUSIONS

The focus of this paper is a new JET database detailing the pedestal structure and pedestal evolution for ITER relevant, high triangularity, Type I ELMy H-mode plasmas. This study extends [30], exploiting improvements in diagnostic capabilities, primarily due to the installation of the JET High Resolution Thomson Scattering (HRTS) system in 2005, which measures T_e and n_e pedestal profiles.

The plasmas detailed are single null, neutral beam heated and gas fuelled with an average plasma triangularity of ~ 0.41 . There is minimal degradation of plasma performance up to $n_{e,\text{ped}}/n_{\text{GW}} \sim 1.0$. In the past maintaining good performance at high fuelling has been difficult although, as shown by the new database and [30], it is possible with a large degree of plasma shaping. Further still at high fuelling ($\Gamma_D = 2.6 \times 10^{22}$ el/s), corresponding to a normalised pedestal density $n_{e,\text{ped}}/n_{\text{GW}} \sim 1.0$, the performance increases as shown by both H_{98} and the stored thermal energy. This is due to an increase in pedestal performance, as shown by the pedestal stored energy.

A mixed Type I/II ELM regime, as originally observed by [30], has been re-established on JET where there is an increased loss between the Type I ELMs. Similar to 2002 study the Type I ELM frequency decreases with increasing pedestal density. This is due to the increased inter-ELM loss at higher pedestal density prolonging the build up towards the critical pressure as supported by a difference in the build up of stored energy between a low and high fuelling pulse. Another factor which could influence the ELM frequency, the proximity to the LH threshold, is shown to be constant across the fuelling scan.

Further to [30], this study quantifies the pedestal characteristics throughout the ELM cycle by an mtanh least squares fit to HRTS T_e and n_e profiles. The change in pedestal structure has been verified by a linear least squares fitting routine and although the obtained widths differ in comparison to the mtanh fits the data trends are similar. The pre-ELM temperature, density and pressure pedestal are wider for an example mixed Type I/II ELMy pulse at high fuelling in comparison to a pure Type I ELMy pulse. Also the pre-ELM pedestal pressure is higher for the mixed Type I/II pulse. The pedestal width for the pure Type I ELMy pulse narrows and the peak pressure gradient increases during the ELM cycle, whereas the width and peak pressure gradient saturate for the mixed Type I/II ELMy pulse. The fits to the HRTS profiles act as an input to the stability and predictive pressure pedestal models.

The PB stability analysis produced by MISHKA-1 shows the plasma edge stability for the mixed Type I/II ELMy pulse moves from stable towards unstable, approaching the ideal ballooning limit of the PB stability boundary. The plasma edge stability saturates towards the last 60% of the ELM cycle with the pre-ELM operational point located on the stability boundary. In contrast the plasma edge stability for the pure Type I ELMy pulse becomes progressively more unstable during the ELM cycle as the operational point also approaches the ideal ballooning limit of the stability boundary. The pre-ELM operational point for the pure Type I ELMy pulse is over the stability boundary, deep into the unstable region. A deconvolution technique is used to determine the temperature and density pedestal widths from the HRTS profiles. This technique assumes the

profiles are truly mtanh and is the current leading method of interpreting the JET HRTS profiles. However, the pre-ELM pedestal width for the pure Type I ELM pulse is particularly narrow and approaches the FWHM of the JET HRTS instrument function (11mm for the two pulses shown in Figure 7). This may result in an underestimate of the pedestal width, which is particularly prominent for the temperature pedestal fit as a weighted deconvolution technique is employed [8]. As the systematic errors are difficult to quantify a complete understanding for the pre-ELM operational point being so deeply in the unstable region for the pure Type I ELM pulse is yet to be attained.

EPED, based on a combined PB and KB model, predicts the pre-ELM pedestal pressure and width. On average there is good agreement between experimental measurements and the model where the ratio of predicted pedestal height to observed pedestal height is 1.04 ± 0.22 and the ratio of predicted pedestal width to observed pedestal width is 1.01 ± 0.23 . This spread is within the range of EPED predictive accuracy as observed in a wider multi machine comparison [2, 3, 41]. However there are a number of discrepancies. The observation that the pedestal width becomes narrower during the ELM cycle suggests that the pressure gradient may not approach KB mode criticality until the latter part of the ELM cycle. If the pressure gradient is limited by KB modes throughout the ELM cycle, the pedestal is expected to widen during the ELM cycle as β_{pol} increases, as is observed in DIII-D [11, 22] and MAST [5, 6]. This is discussed further in [Saarelma submitted to Nuclear Fusion] which presents a detailed gyrokinetic analysis of the pure Type I ELM pulse and mixed Type I/II pulses presented in this paper.

Furthermore, the pre-ELM pedestal width as predicted by EPED does not vary as strongly as observed in the new JET fuelling scan. The experimental pre-ELM profile widths from the mtanh fits are $\Delta_{n_e} = 1.5 \pm 0.1 \text{ cm}$ and $\Delta_{T_e} = 1.9 \pm 0.1 \text{ cm}$ for a low fuelling plasma and $\Delta_{n_e} = 2.1 \pm 0.1 \text{ cm}$ and $\Delta_{T_e} = 2.9 \pm 0.1 \text{ cm}$ for a high fuelling plasma. This corresponds to an increase, in real space, of 40% for the density pedestal width and 53% for the temperature pedestal width from the pure Type I to mixed Type I/II ELM pulse. Using the expression $\Delta = (\Delta_{T_e} + \Delta_{n_e})/2$ and converting to normalised poloidal flux coordinates (Ψ) the experimental measurements show an increase in pedestal width from $\Delta_{\Psi} = 0.034$ to $\Delta_{\Psi} = 0.053$ corresponding to an increase of $\sim 55\%$ from low to high fuelling. Moreover the experimental pre-ELM pressure pedestal height increases by $\sim 20\%$ for a high fuelling pulse in comparison to low fuelling pulse. The wider pre-ELM pedestal found for the mixed Type I/II ELM pulse in comparison to the pure Type I ELM pulse facilitates an increase in pedestal pressure as the steep edge gradient can be sustained over a larger region. This is in spite of a 21% reduction of the peak pressure gradient. In contrast EPED, given the eight scalar input parameters (B_t , I_p , R , a , δ , κ , $n_{e,ped}$ and $\beta_{N,global}$), predicts a decrease of 25% in pedestal pressure and a decrease in pedestal width of 20% in poloidal flux space going from the pure Type I to mixed Type I/II ELM pulse. The disagreement between experiment and EPED has two possible explanations. First if we speculate EPED, like MISHKA-1, under-predicts the critical density, which marks the transition from kink-peeling to ballooning limited plasmas, this will account for

opposing trends in pedestal pressure. The critical density is a strong function of Z_{eff} , plasma shape and is strongly dependent on the accuracy of neoclassical bootstrap current models. Second, the stronger broadening of the experimental pedestal width than predicted by EPED is an indication that other transport related processes contribute to defining the pedestal width such as enhanced inter-ELM transport as observed at high fuelling, for mixed Type I/II ELMy pulses.

ACKNOWLEDGEMENTS

This work was supported by EURATOM and carried out within the framework of the European Fusion Development Agreement. The views and opinions expressed herein do not necessarily reflect those of the European Commission.

REFERENCES

- [1]. Beurskens M.N.A., et al. *Pedestal and scrape-off layer dynamics in ELMy H-mode plasmas in JET*. Nuclear Fusion, **49**:125006, 2009.
- [2]. Beurskens M.N.A., et al. *H-mode pedestal scaling in DIII-D, ASDEX Upgrade, and JET*. Physics of Plasmas, **18**:056120, 2011.
- [3]. Beurskens M.N.A., et al. *Comparison of hybrid and baseline ELMy H-mode confinement in JET with the carbon wall*. Nuclear Fusion, **53**:013001, 2013.
- [4]. Connor J.W. et al. *Magnetohydrodynamic stability of tokamak edge plasmas*. Physics of Plasmas, **5**:2687, 1998.
- [5]. Dickinson D., et al. *Towards the construction of a model to describe the inter-ELM evolution of the pedestal on MAST*. Plasma Physics and Controlled Fusion, **53**:115010, 2011.
- [6]. Dickinson D. et al. *Kinetic instabilities that limit b in the edge of a tokamak plasma: a picture of an H-mode pedestal*. Physical Review Letters, **108**:135002, 2012.
- [7]. Dodt, D et al. *Results from the upgraded Lithium Beam Diagnostic for the Pedestal Densities in JET L and H-mode Plasmas*. Proc. 39th European Physical Society Conference on Plasma Physics (Stockholm, Sweden, 2012).
- [8]. Frassinetti L., et al. *Spatial resolution of the JET Thomson scattering system*. Review of Scientific Instruments, **83**:013506 – 013506–10, 2012.
- [9]. Giroud C., et al. *Integration of a radiative divertor for heat load control into JET high triangularity ELMy H-mode plasmas*. Nuclear Fusion, **52**:063022, 2012.
- [10]. Groebner R.J., et al. *Temporal evolution of H-mode pedestal in DIII-D*. Nuclear Fusion, **49**:045013, 2009.
- [11]. Groebner R.J., et al. *Limits to H-mode pedestal pressure gradient in DIII-D*. Nuclear Fusion, **50**:064002, 2010.
- [12]. Huysmans G.T.A. et al, Computational Physics : Proc. Int. Conf. (Amsterdam, 1991) (Singapore : World Scientific)
- [13]. ITER H-mode database working group. *ITER H mode confinement database update*, Nuclear Fusion, **34**:131, 1994.

- [14]. ITER Physics Basis. *Chapter 1: Overview and summary*. Nuclear Fusion, **39**:2137, 1999.
- [15]. ITER Physics Basis. *Chapter 1: Overview and summary*. Nuclear Fusion, **47**:S1–S17, 2007.
- [16]. ITER Physics Basis. *Chapter 2: Plasma confinement and transport*. Nuclear Fusion, **47**:S18–S127, 2007.
- [17]. Maddison G., et al. *Demonstration of real-time control of impurity seeding plus outboard strike-point sweeping in JET ELMy H-mode plasmas*. Nuclear Fusion, **51**:082001, 2011.
- [18]. Martin Y.R., et al. *Power requirements for accessing the H-mode in ITER*, Journal of Physics: Conference Series, 123:012033, 2008. 11th IAEA Technical Meeting on H-mode Physics and Transport Barriers.
- [19]. Mikhailovskii A.B., et al. *Generalized MHD for numerical stability analysis of high-performance plasmas in tokamaks*. Plasma Physics Reports. **23**:844, 1997.
- [20]. Miller R.L., et al. *Noncircular, finite aspect ratio, local equilibrium model*. Physics of Plasmas, **5**:973, 1998.
- [21]. Nunes I., et al. Proc. 23rd Int. Conf. on Fusion Energy 2010 (Daejeon, South Korea, 2010) (Vienna: IAEA) EXC/P8–03.
- [22]. Osborne T.H., et al. *Scaling of H-mode pedestal and ELM characteristics from a multi-tokamak database and comparison to theoretical models*. Proc. 13th Int. Workshop on H-mode Physics and Transport Barriers (Oxford, UK, 2011) P3.15
- [23]. Pamela J., et al. *Overview of JET results, near term plans*. Fusion Engineering and Design, **43**:1540–1554, 2003.
- [24]. Pasqualotto R., et al. *High resolution thomson scattering for joint european torus (JET)*, Review of Scientific Instruments, **75**:3891–3893, 2004. 15th Topical Conference on High-Temperature Plasma Diagnostics, (San Diego, US, 2004).
- [25]. Perez C.P., et al. *Washboard modes as ELM-related events in JET*. Plasma Physics and Controlled Fusion, **46**:61–87, 2004.
- [26]. Perez C.P., et al. *Identifying the MHD signature and power deposition characteristics associated with type-II ELMs in ASDEX Upgrade*, Plasma Physics and Controlled Fusion, vol. **50**, 065018, 2008.
- [27]. Philipps V., et al. *Overview of the JET ITER-like Wall Project*. Fusion Engineering and Design, **85**:1581–1586, 2010.
- [28]. Saarelma S., et al. *MHD stability analysis of small ELM regimes in JET*. Plasma Physics and Controlled Fusion, **51**:035001, 2009.
- [29]. Saarelma S., et al. *MHD and gyro-kinetic stability of JET pedestals*. Submitted to Nuclear Fusion, accessed 15 Jan 2013, <<http://arxiv.org/abs/1301.2919>>
- [30]. Saibene G., et al. *Improved performance of ELMy H-modes at high density by plasma shaping in JET*. Plasma Physics and Controlled Fusion, **44**:1769, 2002.
- [31]. Sartori R., et al. *Edge operational space for high density/high confinement ELMy H-modes in JET*. Plasma Physics and Controlled Fusion, **44**:1801–1813, 2002.

- [32]. Sartori R., et al. *Study of Type III ELMs in JET*. Plasma Physics and Controlled Fusion, **46**:723–790, 2004.
- [33]. Sauter O. and Anglioni C. *Neoclassical conductivity and bootstrap current formulas for general axisymmetric equilibria and arbitrary collisionality regime*. Physics of Plasmas, **6**:2834–2839, 1999.
- [34]. Scannell R. et al. *Deconvolution of Thomson scattering temperature profiles*. Review of Scientific Instruments, **82**:053501, 2011.
- [35]. Schneider P.A., et al. *Characterization of the ELM Synchronized Edge Pedestal in AUG, DIII-D and JET*, Proc. 13th International Workshop on H-mode Physics and Transport Barriers, (Oxford, 2011).
- [36]. Snyder P.B. et al. *Edge localized modes and the pedestal: A model based on coupled peeling–ballooning modes*. Physics of Plasmas, **9**:5, 2002.
- [37]. Snyder P.B., et al. *Stability and dynamics of the edge pedestal in the low collisionality regime: physics mechanisms for steady–state ELM–free operation*. Nuclear fusion, **47**:961–968, 2007.
- [38]. Snyder P.B., et al. *Development and validation of a predictive model for the pedestal height*. Physics of Plasmas, **16**:056118, 2009.
- [39]. Snyder P.B., et al. *The EPED Pedestal Model: Model Extensions and Validation*, Proc. 13th International Workshop on H-mode Physics and Transport Barriers, (Oxford, 2011).
- [40]. Snyder P.B., et al. *A first principles predictive model of the pedestal height and width: development, testing and ITER optimization with the EPED model*. Nuclear fusion, **51**:103016, 2011.
- [41]. Snyder P.B., et al. *The EPED Pedestal Model: Application to ELM–Suppressed Regimes, and ITER Predictions*, Proc. 24th IAEA Plasma Physics Conference, (San Diego, 2012).
- [42]. Snyder, P.B. et al. *The EPED pedestal model and edge localized mode–suppressed regimes: Studies of quiescent H–mode and development of a model for edge localized mode suppression via resonant magnetic perturbations*. Physics of Plasmas **19**:056115, 2012.
- [43]. Wilson H.R., et al. *Numerical studies of edge localized instabilities in tokamaks*. Physics of Plasmas, **9**:4, 2002.
- [44]. Wolfrum E., et al. *Characterization of edge profiles and fluctuations in discharges with type–II and nitrogen–mitigated edge localized modes in ASDEX Upgrade*. Plasma Physics and Controlled Fusion, **53**:085026, 2011.

	2002	Current
$(\delta_{\text{up}} + \delta_{\text{low}})/2 = \delta$	$(0.49 + 0.45)/2 = 0.4$	$(0.43 + 0.39)/2 = 0.41$
I_p/B_t	2.5MA/2.7T	2.5MA/2.7T
P_{NBI}	< 15MW	< 15MW
Γ_D	$0-5 \times 10^{22}$ e1/s	$0.2-6.1 \times 10^{22}$ e1/s
Divertor Config.	Septum Divertor (Carbon)	LBSRP Divertor (Carbon)

Table 1: Comparison of plasma scenario for 2002 and present day scenario. The current divertor configuration is termed Load Bearing Septum Replacement Plate (LBSRP) [23].

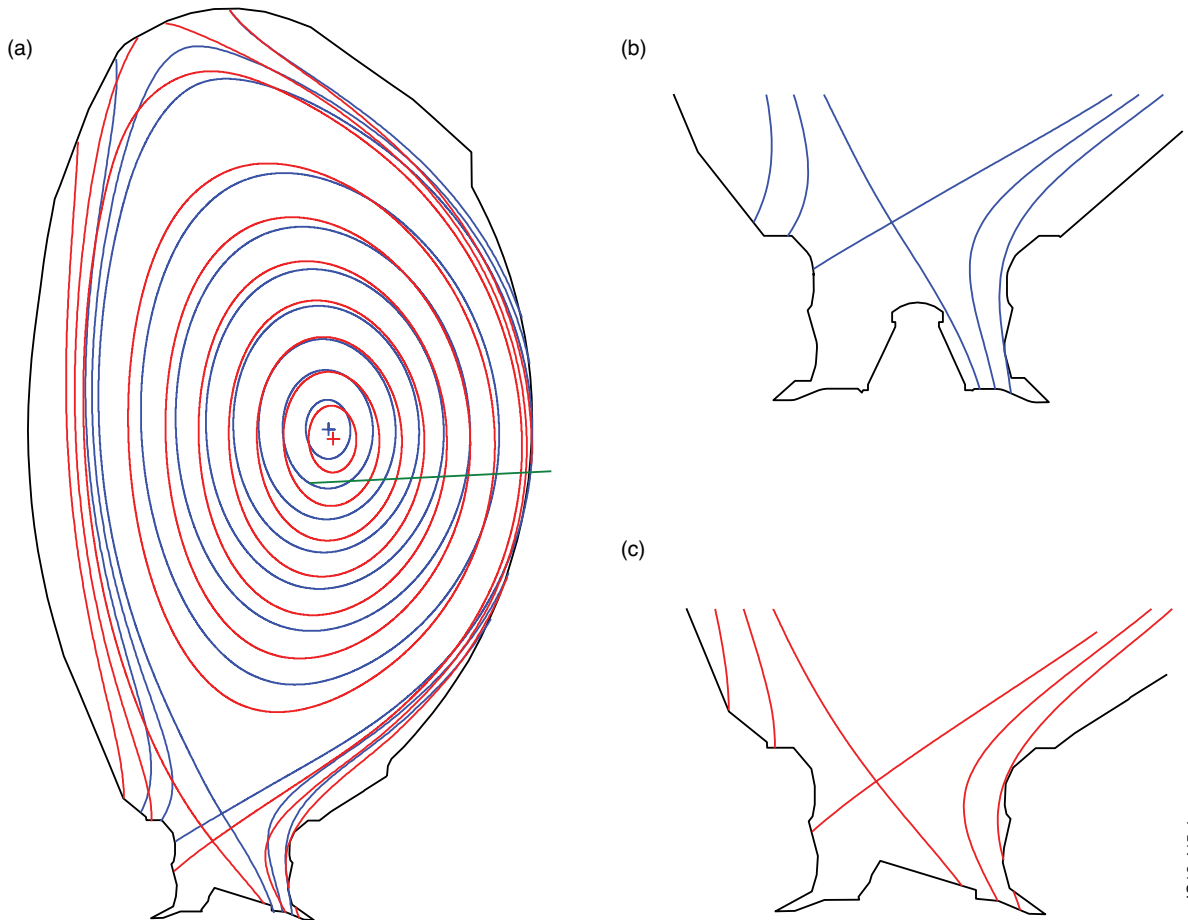


Figure 1: a) Comparison of EFIT equilibrium reconstruction for JET Pulse No: 52014 blue line ($t = 23.1s$) [30] and JET Pulse No: 79503 red line ($t = 22.0s$) where the green line is the HRTS line-of-sight. Divertor configuration for b) JET Pulse No: 52014 (Septum Divertor) and c) JET Pulse No: 79503 (LBSRP Divertor).

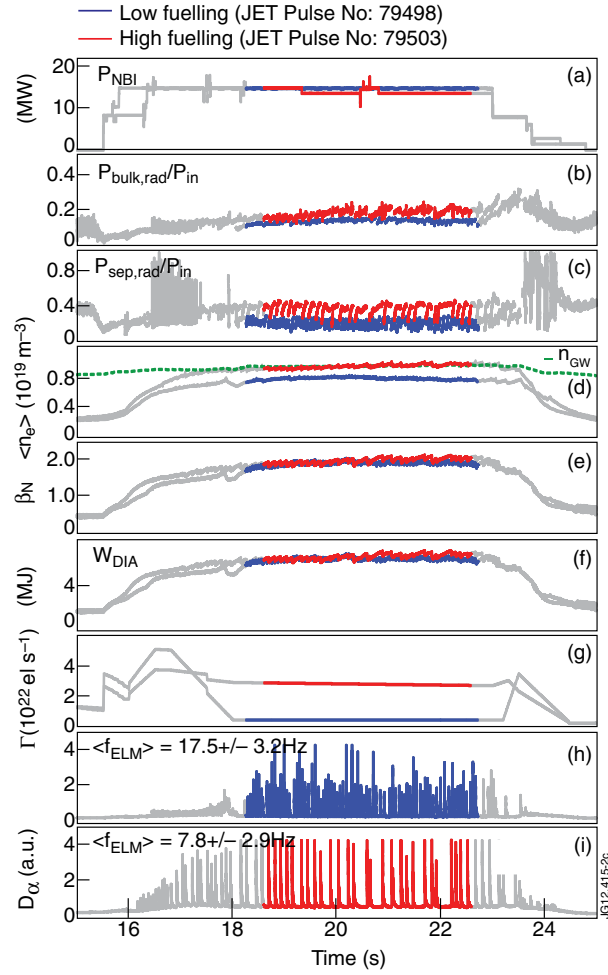


Figure 2: Low (blue) and high (red) fuelling pulses showing a) NBI power, b) bulk radiated power fraction, c) separatrix radiated power fraction, d) line averaged density n_e and n_{GW} , e) normalised toroidal beta, f) stored energy, g) gas fuelling rate, h) D_α emission for low fuelling and i) D_α emission for high fuelling.

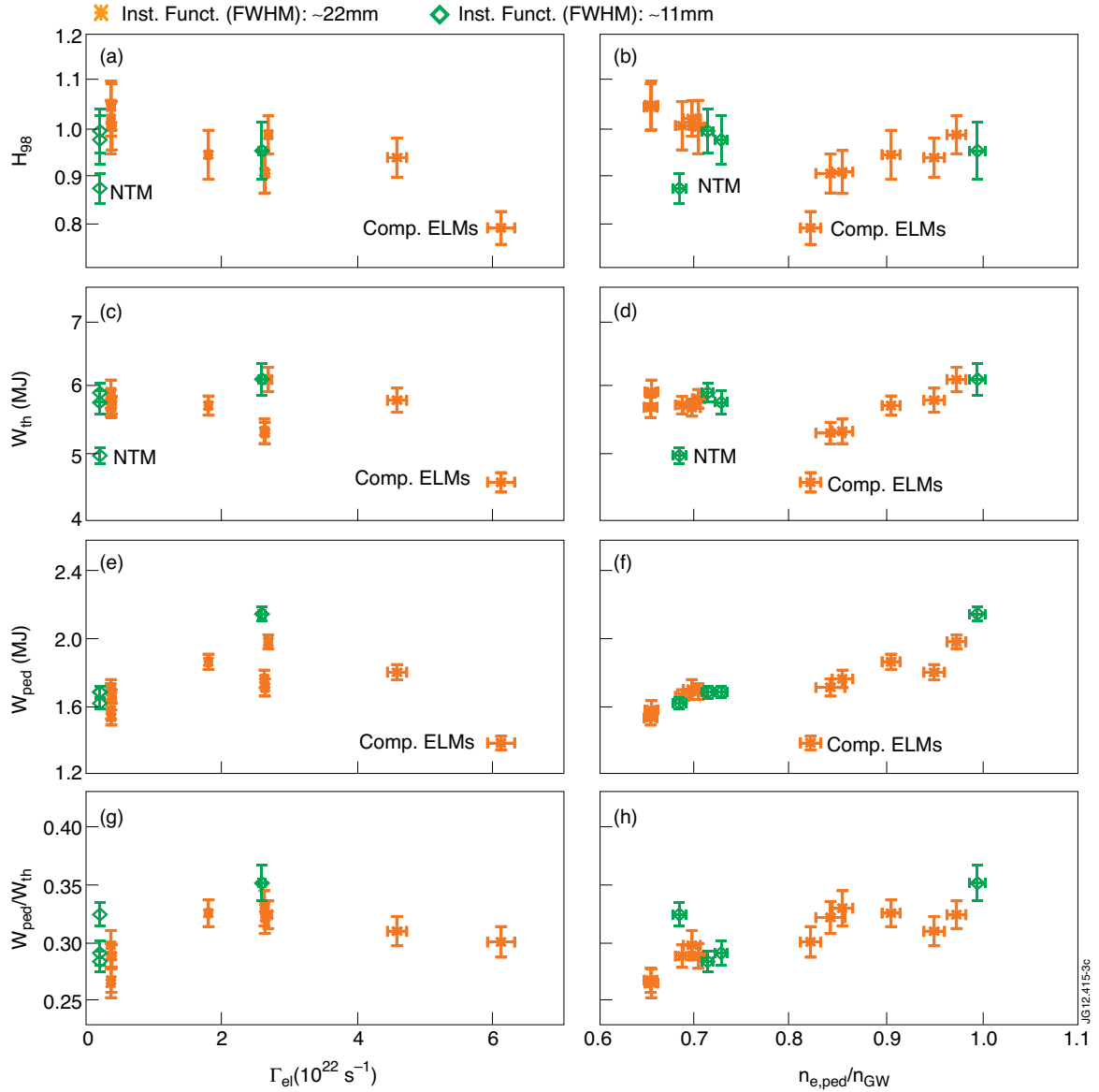


Figure 3: H_{98} as a function of a) fuelling rate and b) pedestal density. Total stored thermal energy (W_{th}) as a function of c) fuelling rate and d) pedestal density. Pedestal stored energy (W_{ped}) as a function of e) fuelling rate and f) pedestal density. Ratio of pedestal stored energy to total stored thermal energy (W_{ped}/W_{th}) as a function of g) fuelling rate and h) pedestal density. Figure 2 distinguishes between pulses with low (orange) and high (green) resolution HRTS data. As labelled there is one pulse with a Neo-classical Tearing Mode (NTM) resulting in a decrease ($\sim 10\%$) in H_{98} . The pulse labelled Comp. ELMs has a compound ELM regime.

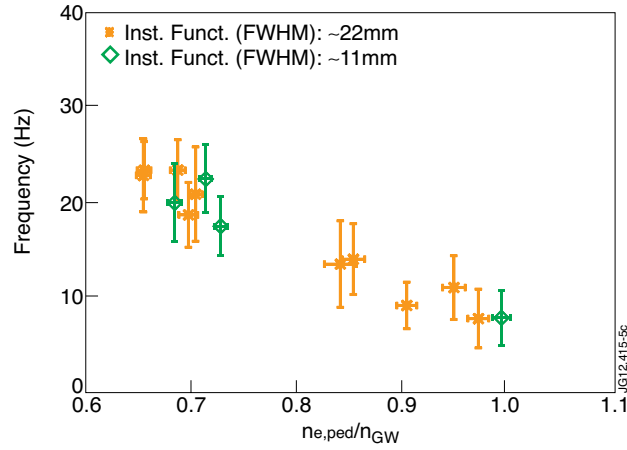


Figure 4: ELM frequency as a function of pedestal density normalised to the Greenwald density.

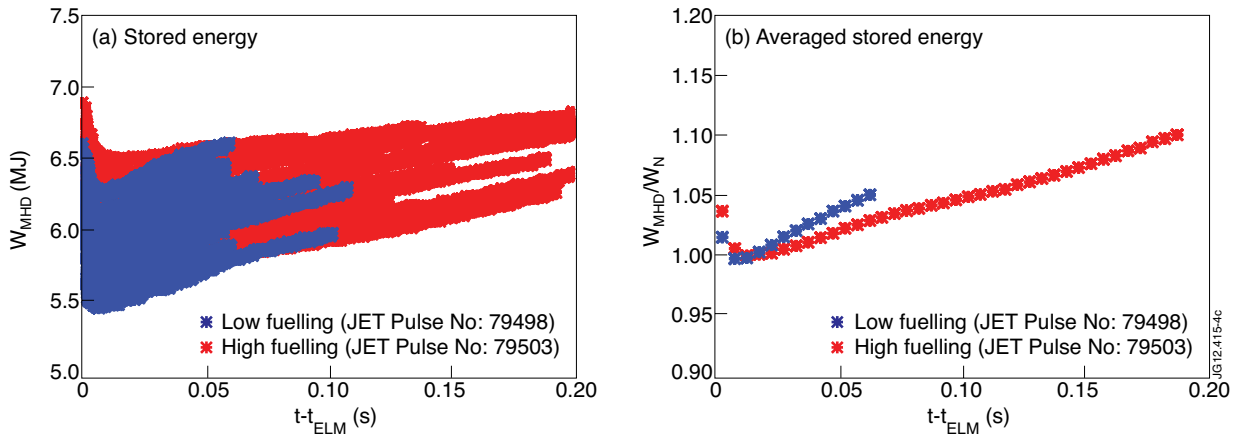


Figure 5: Build-up of stored energy (W_{MHD}) for the low and high fuelling cases as a function of time from the previous ELM. a) shows the ELM synchronised data and b) shows the result of first normalising the ELM synchronised data to a 5-10ms post-ELM window and then applying a moving average.

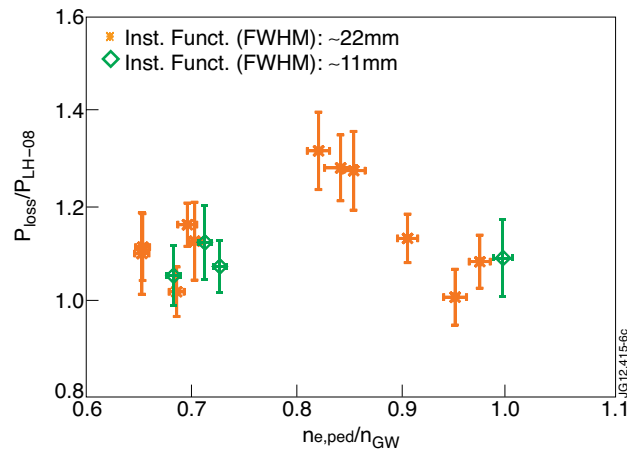


Figure 6: Ratio of P_{loss} to P_{LH-08} as a function of pedestal density normalised to Greenwald density where the ELM dependent parameter dW/dt is averaged over 70-99% of ELM cycle during steady state phase of pulse.

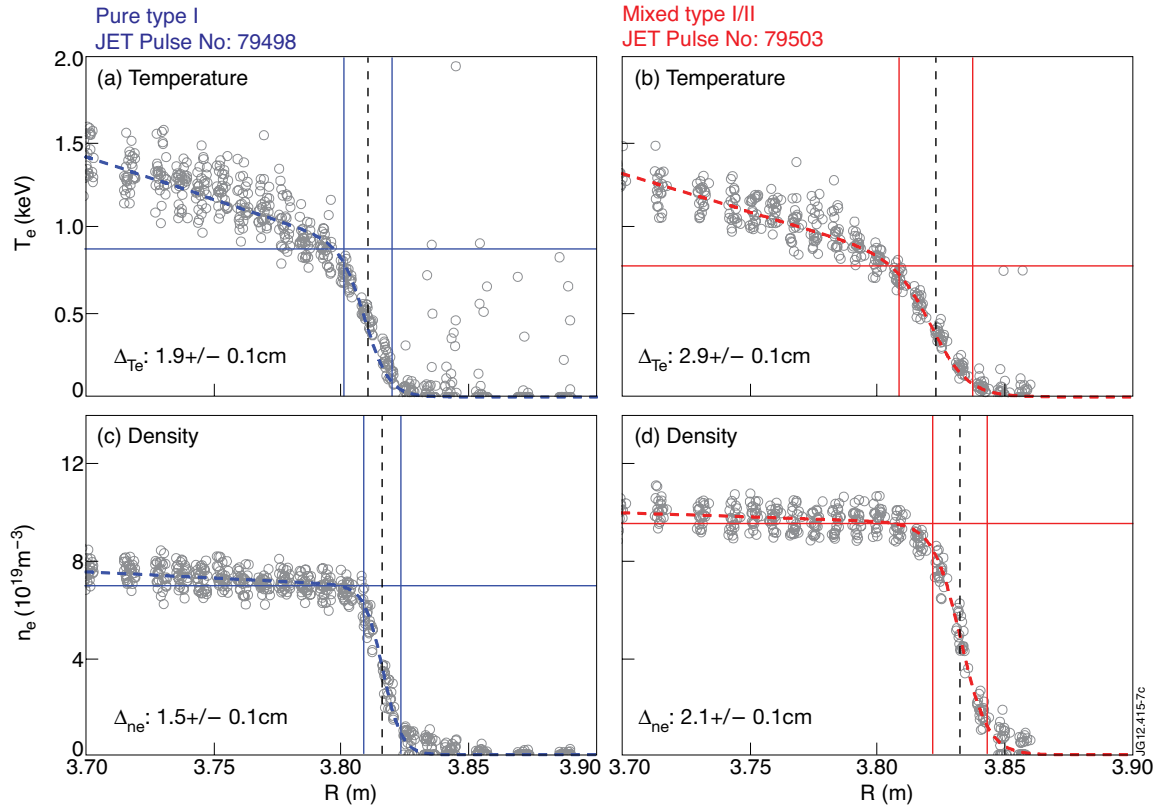


Figure 7: Example of *mtanh* fits for temperature and density JET HRTS profiles for a, c) low (blue) and b, d) high (red) fuelling pulses.

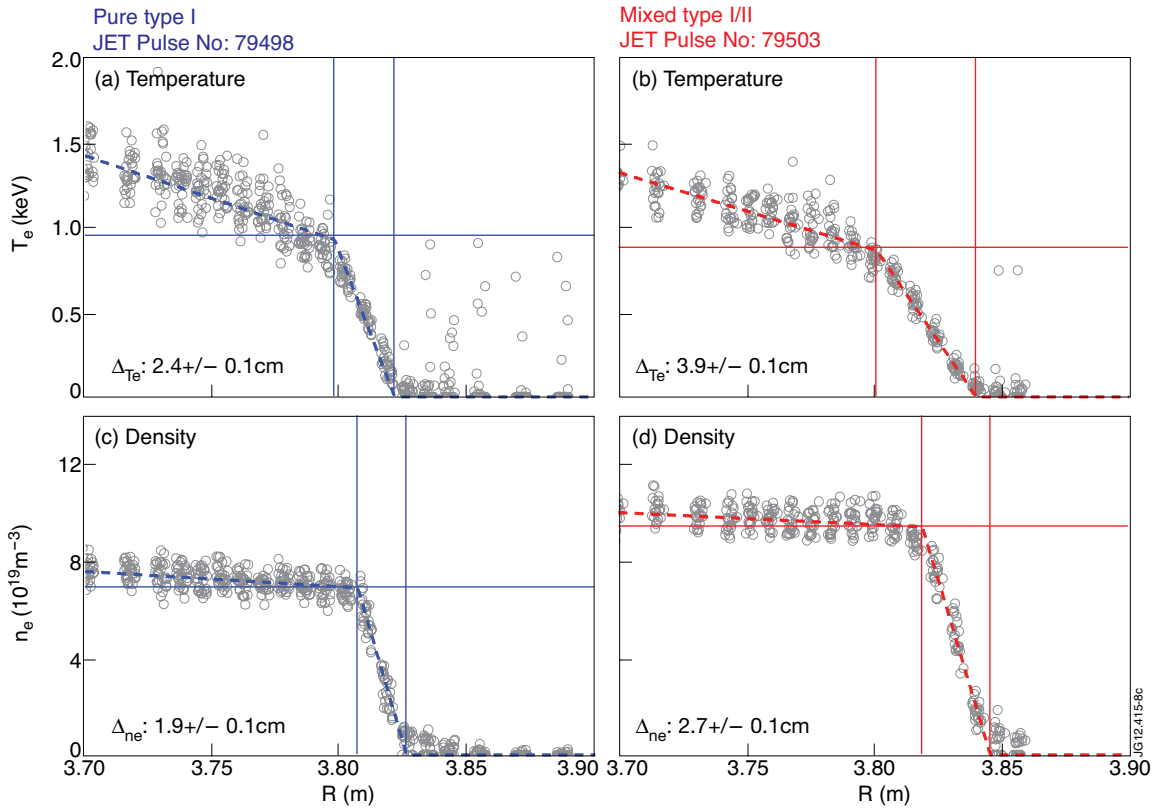


Figure 8: Example of linear fits for temperature and density JET HRTS profiles for a, c) low (blue) and b, d) high (red) fuelling pulses.

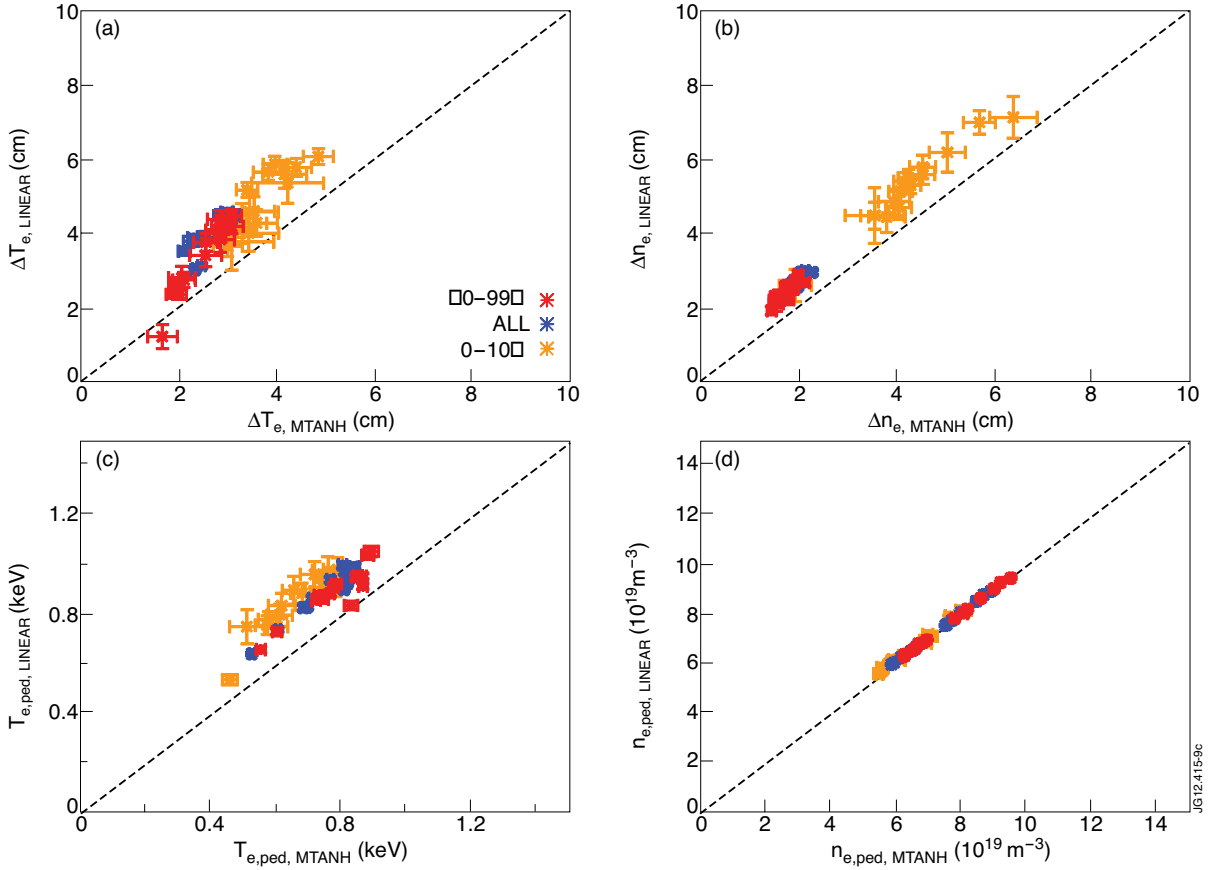


Figure 9: Comparison of linear and mtanh fit results for a) temperature pedestal width, b) the density pedestal width, c) the temperature pedestal height and d) the density pedestal height for all pulses within the new JET fuelling database.

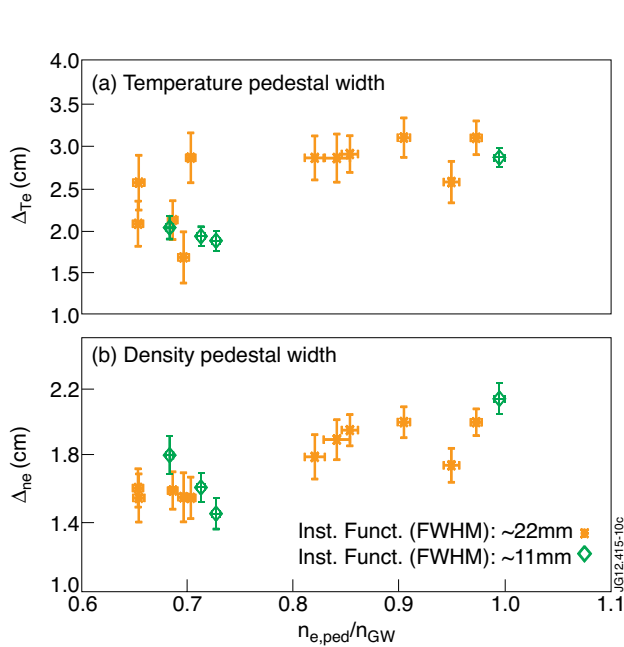


Figure 10: a) Temperature pedestal width and b) density pedestal width as a function of density pedestal height normalised to Greenwald density. Pedestal widths determined from mtanh fits.

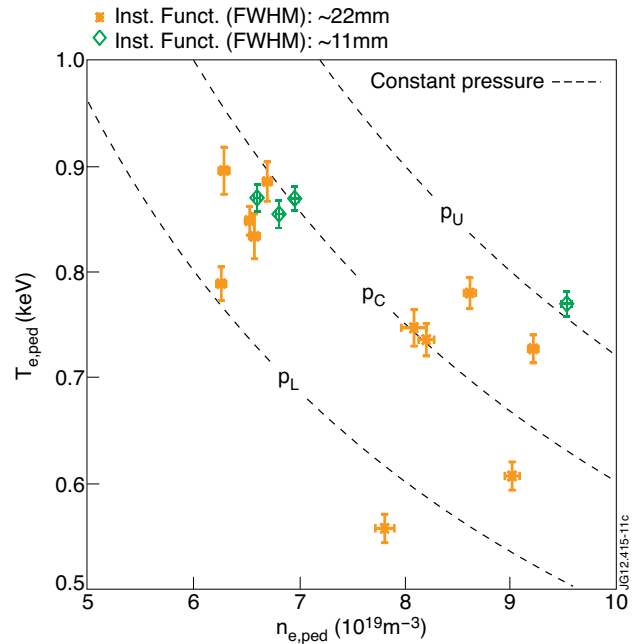


Figure 11: Pedestal temperature versus pedestal density for all 15 discharges within the new fuelling database. There are three isobars indicated by black dashed lines. p_C is the central isobar. The lower isobar, p_L is a 20% decrease with respect to p_C and the upper isobar, p_U a 20% increase, also with respect to p_C .

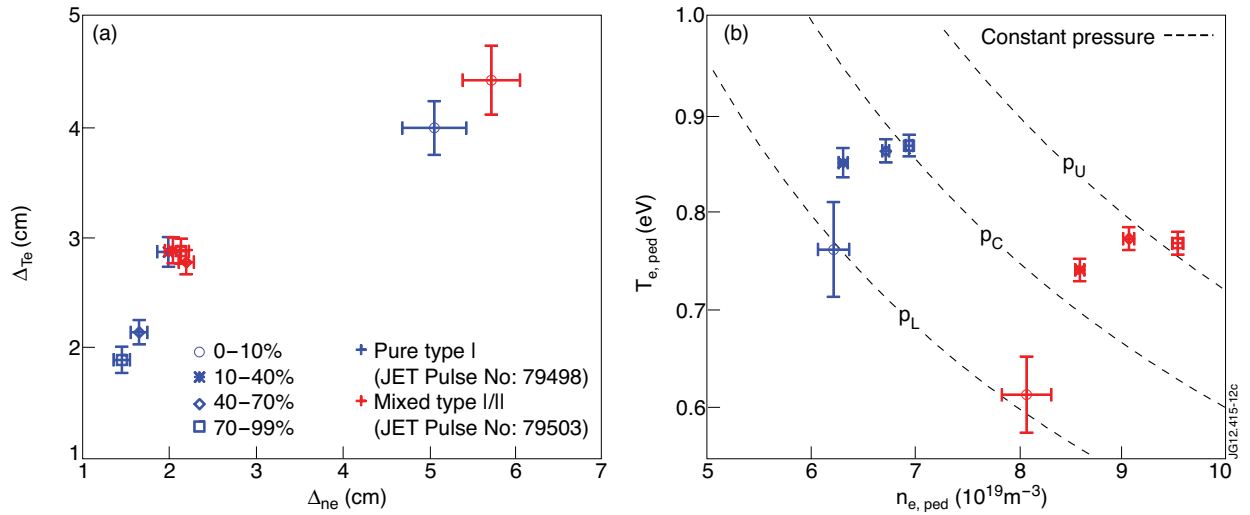


Figure 12: Evolution of a) temperature and density pedestal width, and b) temperature and density pedestal height for low (blue) and high (red) fuelling pulses. Identical to Figure 10, there are three isobars indicated by black dashed lines. p_C is the central isobar. The lower isobar, p_L is a 20% decrease with respect to p_C and the upper isobar, p_U a 20% increase, also with respect to p_C .

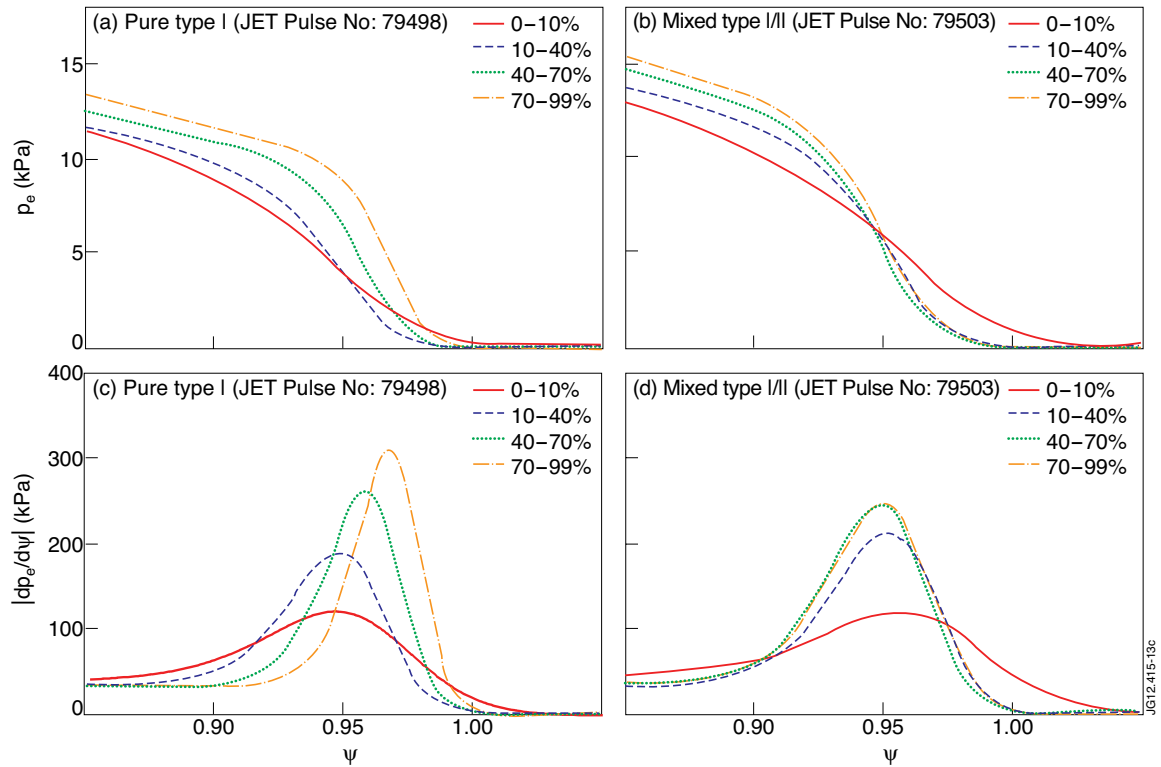


Figure 13: a, b) Pressure profiles and c, d) derivative of pressure profiles corresponding to 0-10% (red), 10-40% (blue), 40-70% (green) and 70-99% (orange) of the ELM cycle for a, c) pure Type I and b, d) mixed Type I/II JET pulses.

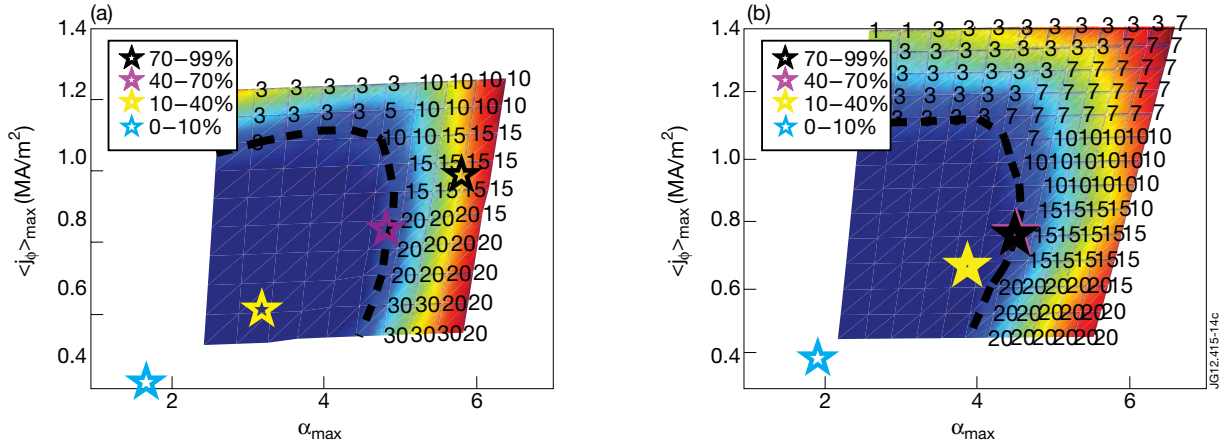


Figure 14: Stability analysis for a) pure Type I (JET Pulse No: 79498) and b) mixed Type I/II (JET Pulse No: 79503) pulse. Analysis performed by MISHKA-1, using \tanh fits to HRTS T_e and n_e profiles as an input.

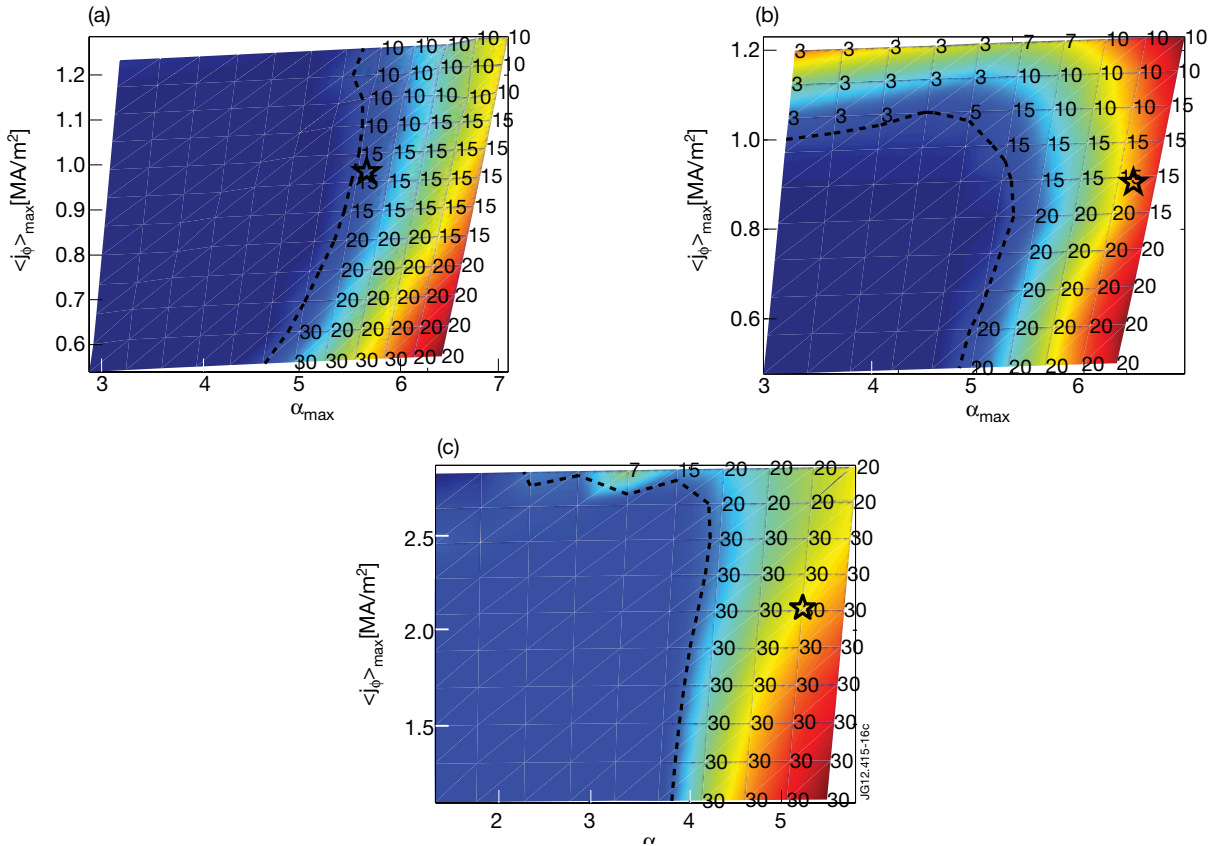


Figure 15: Variation in PB stability analysis when a) applying an inward shift of 0.5% in poloidal flux, b) using $Z_{\text{eff}} = 1$ and c) matching the core and pedestal ion temperature (T_i) gradient. The operation point corresponds to the last 70-99% of the ELM cycle for the pure Type I pulse (JET Pulse No: 79498).

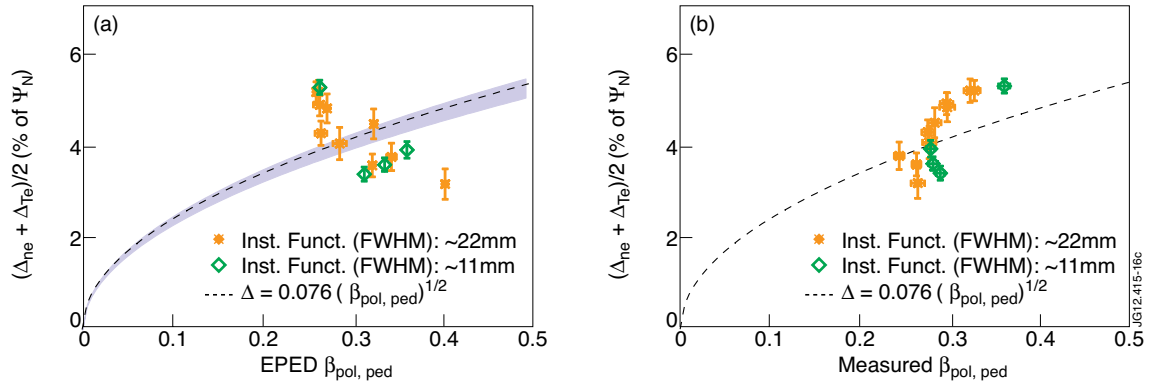


Figure 16: a) Comparison of EPED1 pedestal width predictions (black dashed line) to experimental width measurements (orange and green points) for all Type I ELMy pulses within the new fuelling database. b) Variation of experimental width measurements as a function of measured $\beta_{pol, ped}$.

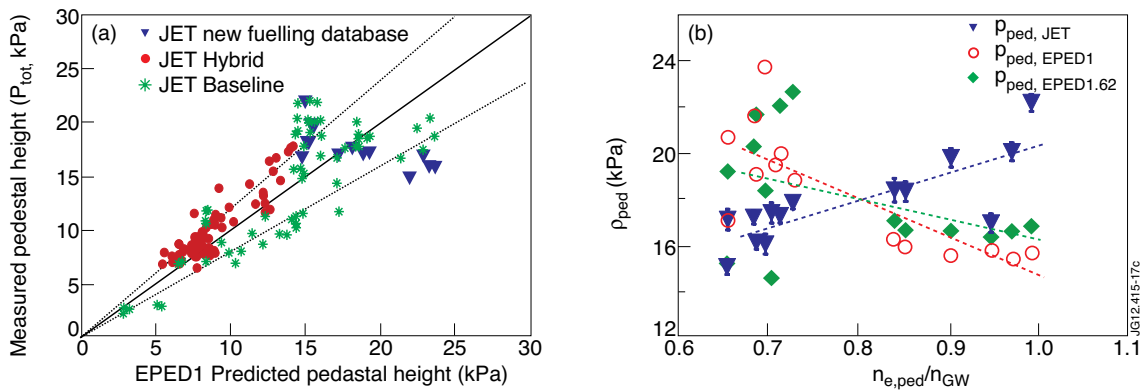


Figure 17: (a) Measured JET pedestal pressure is compared to EPED1 predictions for the new fuelling database (closed blue triangles), as well as previously studied hybrid (red circles) and baseline (green asterisks) cases. (b) For all Type I ELM pulses within the new fuelling database, measured JET pedestal pressure (closed blue triangles), EPED1 predictions (open red circles) and EPED1.62 predictions (closed green diamonds) are shown as a function of pedestal density normalized to Greenwald density.

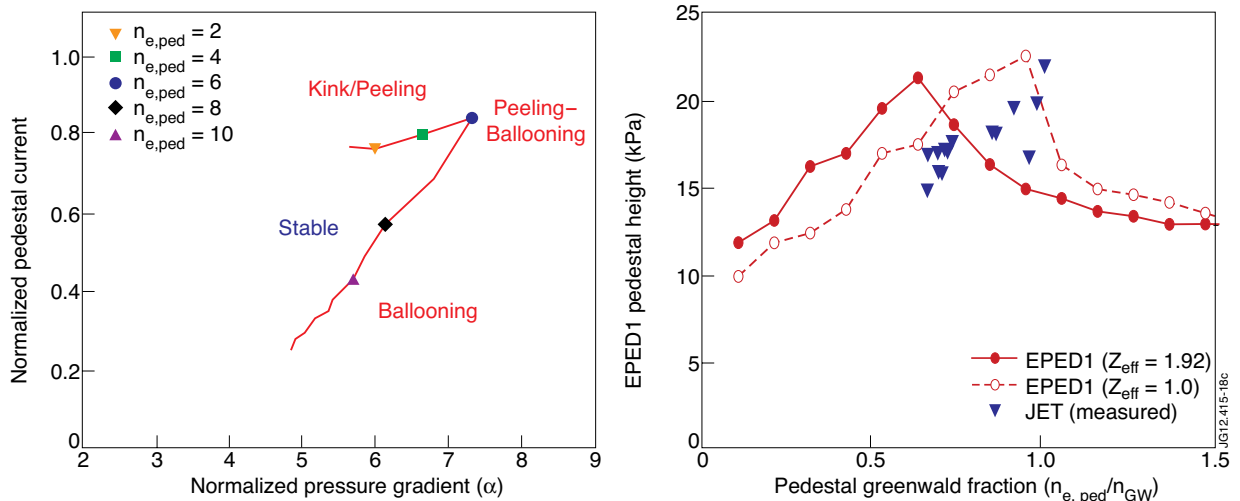


Figure 18: (a) Peeling-ballooning stability diagram, where pedestal density in units of $10^{19} m^{-3}$ is indicated by various symbols along the stability boundary (solid line). As density increases, the limiting instability moves from kink/peeling to peeling-ballooning to nearly pure ballooning modes. (b) EPED1 predicted pedestal pressure as a function of density is shown for the same cases as in (a). Predictions are shown both for $Z_{eff}=1.92$ (solid line) and $Z_{eff}=1$ (dashed line). Measured values (solid triangles) are shown for comparison.